

1 *Research article*

2 **Automated riverbed material analysis using Deep Learning on** 3 **underwater images**

4 Alexander A. Ermilov¹, Gergely Benkő¹ and Sándor Baranya¹

5 ¹Department of Hydraulic and Water Resources Engineering, Budapest University of Technology and Economics,
6 Budapest, 1111, Hungary

7 *Correspondence to:* Alexander A. Ermilov (ermilov.alexander@emk.bme.hu)

8 **Abstract.** The sediment of alluvial riverbeds plays a significant role in river systems both in engineering and
9 natural processes. However, the sediment composition can show great spatial and temporal heterogeneity, even
10 on river reach scale, making it difficult to representatively sample and assess. Indeed, conventional sampling
11 methods in such cases cannot describe well the variability of the bed surface texture due to the amount of energy
12 and time they would require. In this [papermanuscript](#), an attempt is made to overcome this issue introducing a
13 novel image-based, Deep Learning algorithm and related field measurement methodology with potential for
14 becoming a complementary technique for bed material samplings and significantly reducing the necessary
15 resources. The algorithm was trained to recognise main sediment classes in videos that were taken underwater in
16 a large river with mixed bed sediments, along cross-sections, using semantic segmentation. [Videos were taken on](#)
17 [3 different sites in the Upper Section of the Hungarian Danube. One served for training the AI algorithm, while](#)
18 [the other two were for validation.](#) The [introduced](#) method is fast, i.e., the videos of ~~300-400-meter-long~~[300-400-](#)
19 [meter-long](#) sections can be analysed within minutes, with very dense spatial sampling distribution. The goodness
20 of the trained algorithm is evaluated mathematically and via intercomparison with other direct and indirect
21 methods. [The algorithm showed promising results and achieved 70% accuracy: in 19 out of 27 validation point](#)
22 [the AI detection proved to be correct regarding the ratio and percentage of the sediment fractions. Besides, the](#)
23 [spatial trend in the fraction changes was also well captured along the cross-sections, based upon the visual](#)
24 [evaluation of the footages.](#) Suggestions for performing proper field measurements are also given, furthermore,
25 possibilities for combining the algorithm with other techniques are highlighted, briefly showcasing the multi-
26 purpose of underwater videos for hydromorphological [adaptationassessment](#). ~~The papermanuscript is to show the~~
27 ~~potential of underwater videography and Deep Learning through a case study.~~

28 **Keywords:** [rivers](#), [sedimentology](#), [riverbed texture](#), [underwater mapping](#), [sediment classes](#), Artificial Intelligence,
29 Deep Learning, [underwater](#), image-based

30 **1 Introduction**

31 **[1.1 Challenges of riverbed material sampling](#)**

32 The physical composition of a riverbed plays a crucial role in fluvial hydromorphological processes, as a sort of
33 boundary condition in the interaction mechanisms between the flow and the solid bed. Within these processes, the
34 grains on the riverbed are responsible for multiple phenomena, such as flow resistance (Vanoni and Hwang, 1967;
35 Zhou et al., 2021), stability of the [river-bedriverbed](#) (Staudt et al., 2018; Obodovskyi et al., 2020), development

Formatted: Font: (Default) Times New Roman, 10 pt,
Bold, Font colour: Black, Kern at 16 pt

Formatted: Font: (Default) Times New Roman, 10 pt,
Bold, Font colour: Black, Kern at 16 pt

36 of bed armour (Rákóczi, 1987; Ferdowsi et al., 2017; Török et al., 2017), sediment clogging (Rákóczi, 1997; Fetzner
37 et al., 2017), fish shelter (Scheder et al., 2015), etc. Through these physical processes, the bed material
38 composition has a determining effect on numerous river-uses, e.g., possibilities of fluvial navigation, drinking
39 water supply through bank filtration, the quality of riverine habitats, etc. Knowledge of riverbed morphology
40 structure and sedimentgrain composition is therefore of major importance in river hydromorphology. In order to
41 gain information about river-bedriverbed sediments, *in situ* field sampling methodologies are implemented.

42
43 Traditionally, bed material sampling methods are intrusive (i.e., sediment is physically extracted from the bed for
44 follow-up analysis) and carried out via collecting the sediment grains one-by-one (areal, grid-by-number and
45 pebble count methods, see e.g., Bunte and Abt, 2001; Guerit et al., 2018) or in a larger amount by a variety of
46 grab samplers (volumetric methods, such as WMO, 1981; Singer, 2008). This is then followed by measuring their
47 sizes individually on-site or transporting them to a laboratory for mass-sieving analysis (Kellerhals and Bray,
48 1971; Fehr, 1987; Diplas, 1988; Bunte and Abt, 2001). These sampling procedures are time- and energy
49 consuming, especially in large gravel and mixed bed rivers, where characteristic grain sizes can strongly vary both
50 in time and space (Church et al., 1987; Wolcott and Church, 1991; Rice and Church, 1998; USDA, 2007),
51 requiring a dense sampling point allocation. The same goes for critical river reaches, where significant human
52 impact led to severe changes in the morphological state of the rivers (e.g., the Upper-section of the Hungarian
53 Danube; Török and Baranya, 2017). When assessing bed material composition on a river reach scale, experts
54 usually try to extrapolate from the samples, and describe larger regions of the bed (even several thousand m²) by
55 data gathered in a few, several dozen points (see e.g., USDA, 2007; Haddadchi et al., 2018; Baranya et al., 2018;
56 Sun et al., 2021). Gaining a representative amount of the sediment samples is also a critical issue. For instance,
57 following statistical criteria such as those of Kellerhals and Bray (1971) or Adams (1979), a representative sample
58 should weigh ten-to-hundred kg. Additionally, physical bed material sampling methods are unable to directly
59 quantify important, hydromorphological features such as roughness or bedforms (Graham et al., 2005). Due to
60 these constraints, surrogate approaches have recently been intensively tested to analyse the riverbed (see Chapter
61 2). Unlike the conventional methods, these techniques are non-intrusive and rely on computers and other
62 instrumentation to decrease the need of human intervention and speed up the analyses.

63
64 ~~The goal of this papermanuscript is to introduce a Deep Learning-based technique and its first set of results which~~
65 ~~shows potential in complementing the traditional methods, while also providing broader knowledge of the riverbed~~
66 ~~than before through improved (continuous, quick, covering larger areas) data collection. First, a literature review~~
67 ~~is given to better understand the current state of surrogate approaches and their research, gradually leading up to~~
68 ~~the method of this papermanuscript and highlighting its relevance. In the third chapter the case studies and the~~
69 ~~methodology are introduced in details. The third chapter presents the results and their evaluation, followed by a~~
70 ~~discussion about the challenges, the novelty and possible continuations of the method. A brief discussion is also~~
71 ~~given on how the method can support traditional methods and what kind of additional hydromorphological~~
72 ~~parameters can be provided by such videos, uniquely improving the toolkits of sedimentation engineering.~~
73 ~~Finally, the main conclusions of the papermanuscript are drawn.~~

Formatted: Font: (Default) Times New Roman, 10 pt,
Font colour: Black, English (United Kingdom)

1.2 Literature review – surrogate methods

One group of the surrogate approaches is the acoustic methods, where an acoustic wave source (e.g., an Acoustic Doppler Current Profiler; ADCP) is pointed towards the riverbed from a moving vessel, emitting a signal. The strength and frequency of this signal is measured while it passes through the water column, reflecting back to the receiver from the sediment transported by the river, and finally from the riverbed itself. This approach is fast and larger areas can be covered relatively quickly (Guerrero and Lamberti, 2011; Grams et al., 2013). While it has already become widely used for describing sediment movement (i.e., suspended sediment, Guerrero et al., 2016; bedload, Muste et al., 2016; and indirectly flow velocity; Shields and Rigby, 2005; Guerrero et al., 2016; Muste et al., 2016) and channel shape (Zhang et al., 2008), it has not reached similar breakthrough for riverbed material analysis. Researchers found that it is necessary to apply instrument specific coefficients to convert the signal strength, and these coefficients can only be derived by first validating each instrument using collected sediment samples with corresponding ADCP data. Moreover, the method is sensitive to the bulk density of the sediment and to bedforms (Shields, 2010), while it is also not possible to measure individual grains this way (Buscombe et al., 2014a; 2014b). Hence, the separation of surface roughness from the effects of bedforms is also not possible. Clay and silt patches could be separated with the acoustic approach, but gravel could not be distinguished strongly from sand.

Another group of the surrogate approaches is the application of photography (Kellerhals and Bray, 1971; Adams, 1979; Ibbekken and Schleyer, 1986) and later computer vision or image-processing techniques. During the last two decades, two major subgroups emerged: one uses object- and edge detection (by finding abrupt changes in intensity and brightness of the picture, segmenting objects from each other; Butler et al., 2001; Sime and Ferguson, 2003; Detert and Weitbrecht, 2013), and the other one analyses the textural properties of the whole image, using autocorrelation and semi-variance methods to define empirical relationship between image texture and the grain sizes of the photographed sediments (Carbonneau et al., 2004; Rubin, 2004; Verdú et al., 2005). The above-mentioned image processing approaches were very time consuming and required mostly site-specific manual settings, however, a few transferable and more automated techniques have also been developed recently (e.g., Graham et al., 2005; Buscombe, 2013). Even though there is a continuous improvement in the applied image-based bed sediment analysis methods, there are still major limitations the users face with, such as:

- Most of the studies (all the ones listed above) focuses on gravel bed rivers, and only a few exceptions can be found in the literature where sand is also accounted for (texture-based methods; Chezar and Rubin, 2004; Buscombe and Masselink, 2008; Warrick et al., 2009; e.g.: Buscombe, 2013).
- The adaptation environment was typically non-submerged sediment, instead of underwater conditions (a few exceptions: Chezar and Rubin, 2004; Warrick et al., 2009).
- The computational demand of the image processing is high (e.g., one to ten minutes per image; Detert and Weitbrecht, 2013; Purinton and Bookhagen, 2019).
- The analysis requires operator expertise (higher than in case of any conventional method).
- There is an inherent pixel- and image resolution limit (Graham et al., 2005; Buscombe and Masselink, 2008; Buscombe, 2013; Cheng, 2015; Purinton and Bookhagen, 2019). The finer the

113 sediment, the higher resolution of the images should be (higher calculation time), or they must be
114 taken from a closer position (smaller area and sample per image).

115 ~~Due to the limitations above, most of the methods enable the analysis of smaller areas (in the order
116 of ~10 m²) only and are not applicable for quick, continuous measurements of larger regions.~~

117
118 Nowadays, with the rising popularity of Artificial Intelligence (AI), several Machine Learning (ML) techniques
119 have been implemented in image recognition as well.

120
121 The main approaches of segmentation contra textural analysis still remain; however, an AI defines the empirical
122 relationship between the object sizes (Igathinatane et al., 2009; Kim et al., 2020) or texture types (e.g., Buscombe
123 and Ritchie, 2018) in the images and their real sizes. In the field of river sedimentology a few examples can
124 already be found, where ML (e.g., Deep Learning; DL) was implemented. For instance, Rozniak et al. (2019)
125 developed an algorithm for gravel-bed rivers, performing textural analysis. With this approach, ~~information is not
126 gained on individual grains (e.g., their individual shape and position) are not detected~~, but rather the general grain
127 size distribution (GSD) of the whole images. At certain points of the studied river basins, conventional physical
128 samplings (pebble count) were performed to provide real GSD information. Using this data, the algorithm was
129 trained (with ~1000 images) to estimate GSD for the rest of the study site, based on the images. The method
130 worked for areas where grain diameters were larger than 5 mm, and the sediment was well-sorted. The developed
131 method showed sensitivity to sand coverage, blurs, reduced illuminations (e.g., shadows) and white pixels. Soloy
132 et al. (2020) presented an algorithm which used object detection on gravel- and cobble covered beaches to
133 calculate individual grain sizes and shapes. Approximately 50 images were used for the model training, however,
134 the number of images were multiplied with data augmentation (rotating, cropping, blurring the images; see Perez
135 and Wang, 2017) to enhance the learning session and increase the input data. The method was able to reach a
136 limited execution speed of a few seconds per m² and adequately measured the sizes of gravels. Ren et al. (2020)
137 applied an ensemble bagging-based Machine Learning (ML) algorithm to estimate GSD along the 70 km long
138 Hanford Reach of the ~~Columbia river~~Columbia River. Due to its economic importance, a large amount of
139 measurement data has been accumulated for this study site over the years, making it ideal for using ML. By the
140 time of the study, 13,372 scaled images (i.e., their millimetre/pixel ratio was known) were taken both underwater
141 and in the dry zones, covering approx. 1 m² area each. The distance between the image-sampling points was
142 generally between 50-70 m. An expert defined the GSD (8 sediment classes) of each image by using a special,
143 visual evaluation-classification methodology (~~Bovee, 1982~~, Delong and Brusven, 1991; Geist et al., 2000). This
144 dataset was fed to a ML algorithm along with their corresponding bathymetric attributes and hydrodynamic
145 properties, simulated with a 2D hydrodynamic model. Then, it was tested to predict the sediment classes based on
146 the hydrodynamic parameters only. The algorithm performed with a mean accuracy of 53%. Even though this
147 method was not image-based (only indirectly, via the origin of the GSD data), it highlighted the possibilities of
148 an AI for a predictive model, using a high-dimensional dataset. Having such a large data of grain size information
149 can be considered exceptional and takes a huge amount of time to gather, even with the visual classification
150 approach they adapted. Moreover, this was still considered spatially sparse information (point-like measurements,
151 1 m² covered area/image dozens of meters away from each other). Buscombe (2020) used a set of 400 scaled
152 images to train a DL algorithm on image texture properties, using another image-processing method (Barnard et

153 al., 2007) for validation. The algorithm reached a good result for not only gravel, but sand GSD calculation as
154 well, outperforming an earlier, but promising, texture-based method (wavelet analysis; Buscombe, 2013). In
155 addition, the method required fewer calibration parameters than the wavelet image-processing approach. The
156 study also foresaw the possibility to train an AI which estimates the real sizes of the grains, without knowing the
157 scale of one pixel (mm/pixel ratio) if the training is done properly. The AI might learn unknown relationships
158 between the texture and sizes if it is provided with a wide variety (images of several sediment classes) and scale
159 (mm/pixel ratio-) of dataset (however, it is also prone to learn unwanted biases). Recently, Takechi et al. (2021)
160 further elaborated on the importance of shadow- detection and removal, using a dataset of 500 pictures for training
161 a texture-based AI, with the help of an object-detecting image-processing technique (Basegrain; Detert and
162 Weitbrecht, 2013).

163
164 The previously presented studies, applying ML and DL techniques, significantly contributed to the development
165 and improvement of surrogate sampling methods, incorporating the great potential in AI. However, there are still
166 several shortcomings to these procedures. Firstly, none of the image-based DL studies used underwater recordings,
167 even though the underwater environment offers completely different challenges. Secondly, the training images
168 were always scaled, i.e., the sizes of the grains could be easily reconstructed, which is again complicated to
169 accomplish in a river. Lastly, they were not adapted for continuous (i.e., spatially dense) measurement, but rather
170 focused on a sparse grid-like approach. The method introduced in this manuscript follows the ML and DL
171 approach as well. The main novelty of our DL and measurement method, however, is that both the training and
172 analysed videos are recorded underwater, continuously along cross-sections of a large river. Furthermore, the
173 training is unsealed, i.e., the camera-riverbed distance could vary while recording the videos, without considering
174 image-scale. Moreover, compared to the relatively low number of training images in most of the above referred
175 studies, we used a very large dataset (~15000) of sediment images for the texture-based AI, containing mostly
176 sand, gravel, cobble, and to a smaller extent: bedrock together with some other, non-sediment related objects.

177 1.2 Aim of the study

178 The method introduced in this paper manuscript follows the ML and DL approach as well. The main novelty of
179 our DL and measurement method, however, is that both the training and analysed videos are recorded underwater,
180 continuously along cross-sections of a large river. Furthermore, the training is unsealed, i.e., the camera-riverbed
181 distance could vary while recording the videos, without considering image-scale. Moreover, compared to the
182 relatively low number of training images in most of the above referred studies, we used a very large dataset
183 (~15000) of sediment images for the texture-based AI, containing mostly: sand, gravel, cobble, and to a smaller
184 extent: bedrock together with some other, non-sediment related objects. The goal of this manuscript is to introduce
185 a riverbed material analysing Deep Learning-based technique and its first set of results which shows potential in
186 complementing the traditional sampling methods, while also providing broader knowledge of the riverbed than
187 before through more extensive data collection. The introduced technique aims to eventually become a tool for
188 exploratory mapping of the riverbed, by detecting sedimentation features (e.g., deposition zones of fine sediment,
189 bed armour) and helping decision making for river sedimentation management. Also, the long-term hypothesis of
190 the authors includes the creation of an image-based measurement methodology, where underwater videos of the
191 riverbed could serve multiple sediment related purposes simultaneously. Part of which is the current approach for

Formatted: Font: Bold, Font colour: Black, Kern at 16 pt

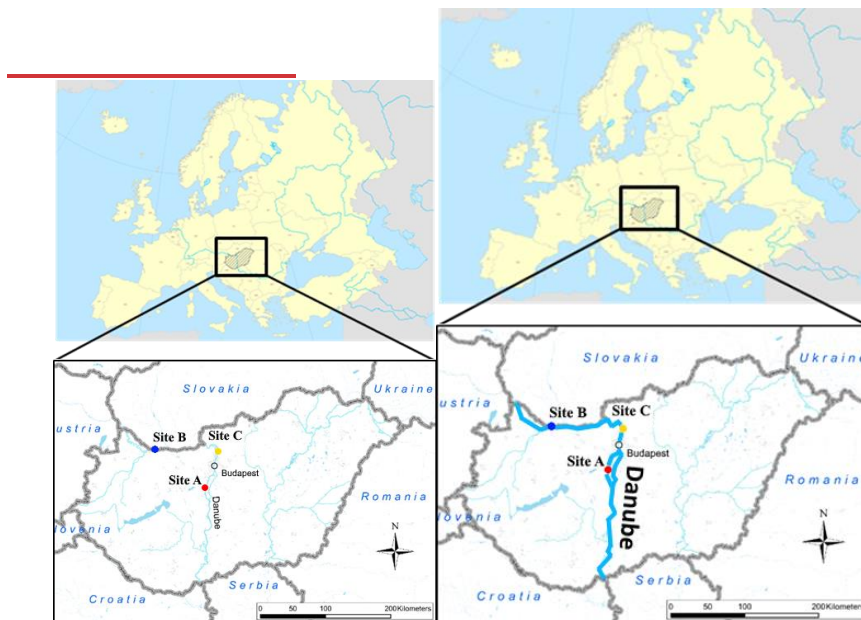
Formatted: Heading 1, Space Before: 24 pt, After: 12 pt, Line spacing: single

192 mapping the riverbed material texture and composition. Others include measuring the surface roughness of the
193 bed (Ermilov et al., 2020) and detecting bedload movement (Ermilov et al., 2022). In this current manuscript, first,
194 a literature review is given to better understand the current state of surrogate bedmaterial sampling approaches
195 and their research, gradually leading up to the method of this manuscript and highlighting its relevance. In the
196 third chapter the case studies and the methodology are introduced in detail. The third chapter presents the results
197 and their evaluation, followed by a discussion about the challenges, the novelty and possible continuations of the
198 method. A brief discussion is also given on how the method can support traditional methods and what kind of
199 additional hydromorphological parameters can be provided by such videos, uniquely improving the toolkits of
200 sedimentation engineering. Finally, the main conclusions of the manuscript are drawn.

202 3 Methods

203 3.1 Case studies

204 The results presented in this study are based on riverbed videos taken during three measurement campaigns, in
205 sections of the ~~Danube river~~ Danube River, Hungary. The first one was at Site A, Ercsi settlement (~ 1606 rkm),
206 the second one was at Site B, Gönyű settlement (~ 1791 rkm), and the third was at Site C, near to Göd settlement
207 (~ 1667 rkm) (Fig. 1).



208 **Figure 1: The location of the riverbed videos, where the underwater recordings took place. (upper section of the**
209 **Hungarian Danube). All sites were located in Hungary, Central Europe. The surveys were carried out on the Danube**
210 **River, Hungary's largest river.**

212 The training of the AI was done using the video images of Site C and a portion of A (test set; see later in Chapter
213 3.3), while Site B and the rest of the images from A served for validation. The measurements were carried out

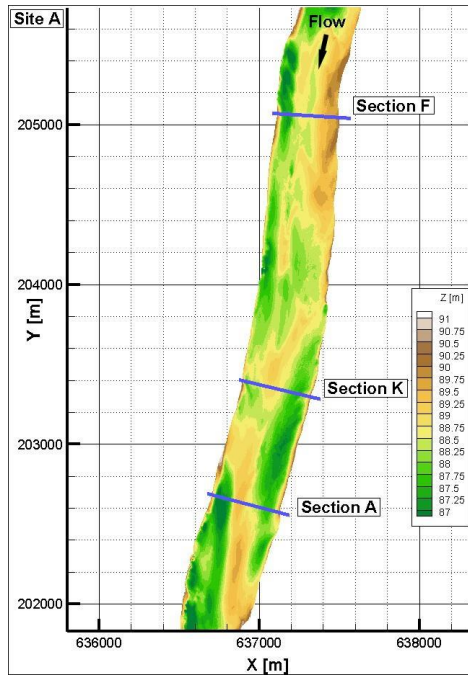
214 during daytime, at mid-water regime ($Q = 1900 \text{ m}^3/\text{s}$) in case of Site A, and low water regime ($Q = 1350 \text{ m}^3/\text{s}$) at
 215 Site B, similarly to Site C ($Q = 700 \text{ m}^3/\text{s}$). This latter site served only for increasing the training image dataset
 216 (i.e., conventional samplings were not carried out at the time of recording the videos), thus we do not go into
 217 further details with it for the rest of the [papermanuscript](#), but the main characteristics are listed in Table 1. As
 218 underwater visibility conditions are influenced by the suspended sediment, the characteristics of this sediment
 219 transport is also included in Table 1 (Q_{susp} - susp. sed. load; SSC – susp. sed. concentration).

220

	Site A	Site B	Site C
Q [m^3/s]	1900	1350	700
B [m]	300 – 450		
H_{mean} [m]	3.5 - 4.5		
S [cm/km]	15		
Characteristic sediment	riverbed gravel, sandy gravel	gravel, gravelly sand	gravel, sandy gravel
Q_{annual,av} [m^3/s]	2000	2200	1400
SSC [mg/l]	25	20	14

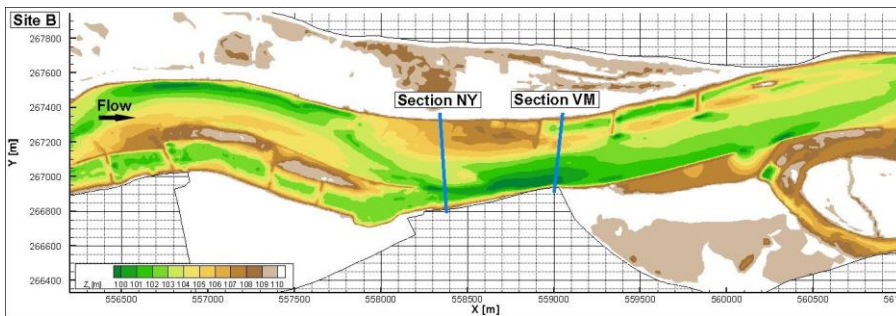
221 Table 1: Main hydromorphological parameters of the measurement sites. Q: discharge during survey; B: river width;
 222 H_{mean}: mean water depth during the survey; S: ~~river-bed~~**riverbed** slope; Q_{annual, av.}: annual-average of the discharge at
 223 the site; SSC: average suspended sediment concentration during the survey.

224 The highest water depths were around 6-7 m in all cases. In Site A, measurements included mapping of the
 225 riverbed with a camera along three separate transects (Fig.2). At Site B, two transects were recorded (Fig.3).



226
227
228
229
230

Figure 2: At Site A, three transects were measured. The vessel moved along these lines from one bank to the other, while carrying out ADCP measurement and recording riverbed videos. Physical bed material samples were also collected in certain points of these sections.



231
232
233
234

Figure 3: At Site B, two transects were measured. The vessel moved along these lines from one bank to the other, while carrying out ADCP measurement and recording riverbed videos. Physical bed material samples were also collected in certain points of these sections.

235 **3.2 Field data collection**

236 **Figure**Fig. 4 presents a sketch of the measurement process with the equipment and a close-up of the underwater
237 instrumentation. During the field measurements, the camera was attached to a streamlined weight (originally used
238 as an isokinetic suspended sediment sampler)-and lowered into the water from the vessel by an electric reel. The
239 camera was positioned perpendicularly to the water and the riverbed, in front of the nose of the weight. Next to
240 the camera, two diving lights worked as underwater light sources, focusing into the camera's field of view (FoV).

241 In addition, four laser pointers were also equipped in hand-made isolation cases to provide possible scales for
242 secondary measurements. They were also perpendicular to the bottom, projecting their points onto the underwater
243 camera field of view. Their purpose was to ensure a visible scale (mm/pixel ratio) in the video footages for
244 validation. During the measurement procedure, a vessel crossed the river slowly through river transects, while the
245 position of the above detailed equipment was constantly adjusted by the reel. Simultaneously, ADCP and RTK
246 GPS measurement were carried out by the same vessel, providing water depth, riverbed geometry, flow velocity,
247 ship velocity and position data. Based on this information and by constantly checking the camera's live footage
248 on deck, the camera was lowered or lifted to keep the bed in camera ~~sight, and~~sight and avoid colliding with it.
249 The sufficient camera – riverbed distance depended on the suspended sediment concentration near the bed and the
250 used illumination. The reel was equipped with a register, with its zero adjusted to the water surface. This register
251 was showing the length of cable already released under the water, effectively the rough distance between the water
252 surface and the camera (i.e., the end of the cable). Of course, due to the drag force this distance was not vertical,
253 but this value could be continuously compared to the water depth measured by the ADCP. Differencing these two
254 values, an approximation for the camera – riverbed distance was given all time. The sufficient difference could
255 be established by monitoring the camera footage while lowering the device towards the bed. This value was then
256 to be maintained with smaller corrections during the survey of the given cross-section, always supported by
257 observing the camera recording, and adjusting to environmental changes. The vessel's speed was also adjusted
258 based on the video and slowed down if the video was blurry or the camera got too far away from the bed (see later
259 in Chapter 4.3). The measurements required three personnel to i) drive the vessel, ii) handle the reel, adjust the
260 equipment position, and monitor the camera footage, iii) monitor the ADCP data, while communicating with the
261 other personnel (see Fig. 4).

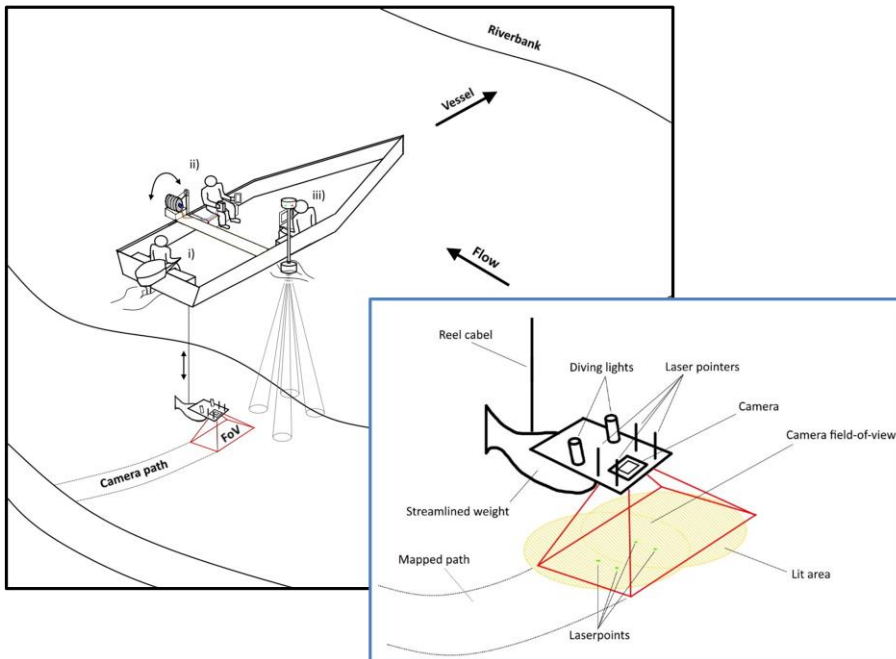


Figure 4: Left: sketch of the measurement process. The vessel was moving perpendicular to the riverbank along a cross-section (i). A reel was used to lower a camera close to the riverbed (ii). Simultaneously, the bed topography and water depth were measured by an ADCP (iii). Right: Close-up sketch of the underwater instrumentation.

The video recordings were made with a GOPRO Hero 7 and a Hero 4 commercial action cameras. Image resolutions were set to 2704x2028 (2.7K) with 60 frame per second (fps) and 1920x1080 (1080p) with 48 fps, respectively. Other parameters were left at their default (see GOPRO 2014; 2018), resulting in slightly different quality of produced images between the two cameras. We found that a 0.2-0.45 m/s vessel speed with 60 fps recording frequency was ideal to retrieve satisfactory images in a range of 0.4-1.6 m camera-bed distances. This meant approximately 15 minutes long measurements per transects. Further attention needs to be paid to the reel and its cable during the crossing when the equipment was on the upstream side of the boat. If the flow velocities are relatively high (compared to the total submerged weight of the underwater equipment), the cable can be pressed against the vessel-body due to the force from the flow itself, causing the reel cable to jump to the side and leave its guide. This results in the equipment falling to the riverbed and the measurement has to be stopped to reinstall the cable. Illumination is also a critical condition for riverbed imaging. Here, a diving light with 1500 lumen brightness and 75° beam divergence, and one with 1800 lumen and 8° were used. The four lasers for scaling had 450-520 nm (purple and green) wavelength and 1-5 mW nominal power. Power supply was ensured with batteries for all instruments.

At Site A and Site B, conventional bed material (physical) samplings were also carried out by a grabbing (bucket) sampler along the analysed transects. At each cross-section had 4-5 samples were taken, with one exception where we had 10. The collected samples were analysed in laboratory by drying, sieving, and weighing to provide local grain size distribution. The measured GSDs were used to validate results of the AI algorithm. Separately, a visual

285 evaluation of the videos was also carried out, where a person divided the transects into subsections based on their
286 dominant sediment classes, after watching the footages.

287 3.3 Image analysis: Artificial Intelligence and the wavelet method

288 A widely used deep neural network architecture was employed in this study, building on former experiences of
289 the authors (Benkő et al., 2020), Google's DeeplabV3+ Mobilnet, in which many novel and state-of-the-art
290 solutions are implemented (e.g., Atrous Spatial Pyramid Pooling; Chen et al., 2018). The model was implemented
291 with Pytorch, exploiting its handy API and backward compatibility. The main goal was to build a deep neural
292 network model which is able to recognise and categorise (via semantic segmentation; Chen et al., 2018) at least
293 three main sediment size classes, i.e., sand, gravel and cobble, in the images, while being quickly deployable. We
294 used our earlier study (Benkő et al., 2020) as a proof-of-concept, where the same architecture was applied for
295 analysing drone videos of a dry riverbed. The benefit of the introduced method compared to conventional imagery
296 methods lies in the potential of automation and increased speed. If the annotation and training is carried out
297 thoroughly, analysing further videos can run effortlessly, while the computation time can be scaled down either
298 vertically (using stronger GPUs) or horizontally (increasing the number of GPUs; if parallel analysis of images is
299 desired). In this study a TESLA K80 24GB GDDR5 348bit GPU, an Intel Skylake Intel® Xeon® Gold 6144
300 Processor (24.75M Cache, 3.50 GHz) CPU with 13GB RAM was used. Also, contrary to other novel image-
301 processing approaches in riverine sediment research (Buscombe, 2013; Detert and Weitbrecht, 2013), the deep
302 convolutional neural network is much less limited by image resolution and mm/pixel ratios, because it does not
303 rely on precise pixel count. This is an important advantage to be exploited here, as we perform non-scaled-training
304 and measurements with the AI, i.e., camera-bed distance constantly ehangedchanged, and size-reference was not
305 used in the images by the AI.

306
307 Fig. 5 presents the flowchart of our AI-based image processing methodology. The first step after capturing the
308 videos-in-the-analysis was to cut the m-captured-videos into frames, during which the videos were exploded into
309 sequential images. Brightening and sharpening filters were applied on the images to improve their quality. Next,
310 the ones with clearest outlines and best visibility were chosen. This selection process was necessary because this
311 way the delineation process (learning the prominent characteristics of each class) can be executed accurately,
312 without the presence of misleading or confusing images, e.g., blurry or dark pictures where the features are hard
313 to recognise. For training purposes, we chose three footages from different sections each being ~15 minutes long
314 with 60 fps and 48 fps, resulting in 129 600 frames. In fact, no such large dataset was needed due to the strong
315 similarity of the consecutive frames. The number of images to be annotated and augmented were therefore
316 decreased to ~2000.

Data creation

- From underwater videos
- Large number of images
- No fix elevation from the river bed
- With multiple frame rate
- Selecting images according to variance and visibility

We also performed a white balance correction on some of the images to improve visibility, making it even easier to later define the sediment class boundaries. We used an additional algorithm to generate more data, with the so-called Simplest Colour Balance method (Limare et al., 2011). It is a simple, but powerful histogram equalisation algorithm which helps to equalise the roughness in pixel distribution.

White balance upgrade

- Separating part of the data and making images more understandable with enhanced white balance
- Improve the visibility of the edges

These steps were followed by the annotation, where we distinguished ten classes. Annotation was carried out by a trained personnel, not by the authors, and performed with the help of an open-source software called

Data annotation

- Separating multiple classes of the sediment
- 10 different classes
- 5 sediment classes and 5 class based on other objects (eg. wood or plastic)

PixelAnnotationTool (Breheret, 2017), which enables the user to colour mask large parts of an image based on colour change derivatives (i.e., colour masking part of the images which belong to the same class, e.g., purple/red – sand, green – gravel, yellow – cobble, etc.). The masks and outlines were drawn manually, together with the so-called-so-called

Data augmentation

- Mirroring and rotating images
- Using Simplest Color Balance, darkening, white balance enhancing, sharpening and blurring to enhance data size

watershed annotation. That is, when a line was drawn, the algorithm checked for similar pixels in the vicinity and automatically annotated them with the same class. The annotation was followed by a data augmentation step where beside mirroring, cropping, rotating the images (to decrease the chance of overfitting), we also convolved them with different filters. These filters added normally distributed noise to the photos to influence the watershed algorithm and applied sharpening, blurring, darkening, and

Training

- On powerful virtual machines with Tesla K80 GPUs
- 80/20 training/test split
- 14784 images were used. 11827 for training and 2957 for validation

white balance enhancement. Thus, at the data level, we tried to ensure that any changes in water purity, light, and transparency, as well as colour changes, were adequately represented during training. Images were uniformly converted to 960x540 resolution, scaling them down to make them more usable to fit in the GPU's memory. The next step was to convert all the images from RGB (Red-Green-Blue) based colour to grayscale. This is important because colour images have 3-channels, so that they contain a red, a green, and a blue layer, while grayscale images' pixel can only take one value between 0 and 255. With this colour conversion we obtained a threefold increase in computational speed. In total, a dataset of 14,784 images was prepared (from the ~2000 images of the 4 training videos). The next step was to separate this into training and validation sets. In this study, approximately 80% of the data was used for training the Artificial Intelligence, while 20% was to validate the training.

Visualization and analysis

- Overall Acc.: 96.38%
- Mean IoU: 41.46%
- Image masks showing the precision visually
- Compare AI generated results with sampled data on new dataset

It was important to mix the images so that the algorithm selects batches in a pseudorandom manner during training, thus preventing the model from being overfitted. Finally, after several changes in the hyperparameters (i.e., tuning), the evaluation and visualisation of the training results were

Figure 5: Flowchart of the applied methodology.

Formatted: Font: (Default) Times New Roman, 9 pt, Bold, English (United Kingdom)

Formatted: Font: (Default) Times New Roman, 9 pt, Bold, English (United Kingdom)

Formatted: Justified

357 performed. Tuning is a general task to do when building Deep Learning Networks, as these hyperparameters
358 determine the structure of the network and the training process itself. Learning rate, for example, describes how
359 fast the network refreshes, updates itself during the training. If this parameter is set too high, the training process
360 finishes quickly, but convergence may not be reached. If it is too low, the process is going to be slow, but it
361 converges. For this reason, nowadays the learning rate decay technique is used, where one starts out with a large
362 learning rate, then slowly reduces it. The technique generally improves optimization and generalization of the
363 Deep Learning Networks (You et al., 2019). In our case, learning rate was initialised to 0.01, with 30000 iteration
364 steps, and the learning rate was reset after every 5000 iterations with a decay of 0.1. A ~~not~~ other important parameter
365 was the batch size, which sets the number of samples fed to the network before it updates itself. Theoretical and
366 empirical evidence suggest that learning rate and batch size are highly important for the generalization ability of
367 a network (He et al., 2019). In our study, a batch size of 16 was used (other general values in the literature are 32,
368 64, 128, 256). We used a cross-entropy loss function.

369
370 As previously mentioned, the training of the AI ~~happened~~ was managed without scaling, and it did not without the
371 need ~~the~~ for equipped lasers. However, we intended to use these laser pointers were used to provide a spatial scale
372 for the recorded videos, as a secondary validation. As the lasers were not functioning as we originally hoped, we
373 could not use them constantly during the cross-sectional surveys and could not aim for transactional scaling and
374 validation this way. Instead, we diverted to validation in the points of the physical samplings as we could use the
375 lasers in a few, selected points only. We used a textural image-processing method to analyse the video images of
376 these ~~e~~-sampling spots, ~~where the physical samples were taken. For~~ For this, the already mentioned, transferable
377 wavelet-based signal- and image-processing method (~~Buscombe, 2013~~) was chosen. The method enables to
378 calculate the image-based grain size distribution of the selected pictures. The grey-scale intensity is analysed
379 through pixel-rows and -columns of the image and handled as individual signals. Then, instead of Fourier-
380 transform, the less-constrained wavelet-transform is applied to decompose them. Finally, calculating the power
381 spectra and the sizes (from pixel to millimetre, using the scale) of the wavelet components (each wavelet describes
382 an individual grain) produces the grain size distribution for the given image. Beforehand, this method was proved
383 to be the most efficient, non-AI image-processing method for mixed sediments (Buscombe, 2013; 2020) and was
384 already tested for underwater circumstances in an earlier study by the authors of present paper manuscript (Ermilov
385 et al., 2020).

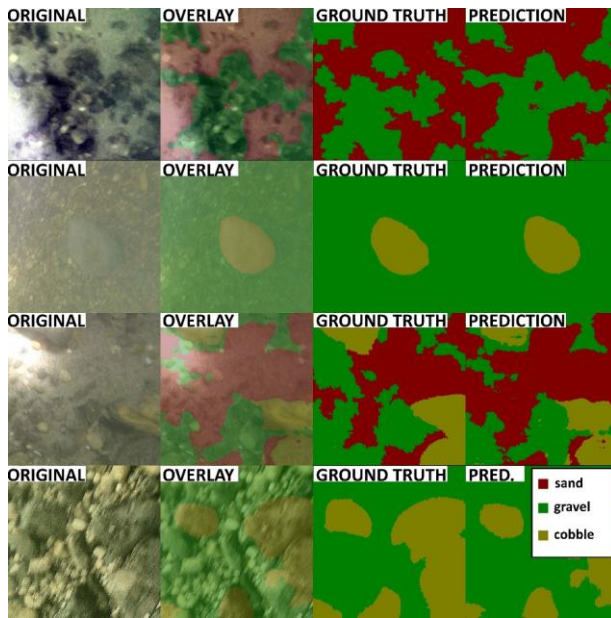
386 4 Results and discussion

387 4.1 Evaluation of the training

388 To evaluate the training process, the image series used for the training was analysed by the developed Deep
389 Learning algorithm. Figure Fig. 65. shows results of original images (from the validation set), their ground truth
390 (annotation by the training personnel), as well as the AI prediction (result of the model). The overlays of the
391 original and the predicted images are also shown for better visualization. Calculating the over-all pixel accuracy
392 (i.e., the percent of pixels that were correctly classified) returned a satisfactory result with an average 96% match.
393 As this parameter in object detection and Deep Learning is not a stand-alone parameter (i.e., it can still be high
394 even if the model performs poorly), the mean IoU (intersection-over-union or Jaccard index) was also assessed,

Formatted: Font: Not Italic

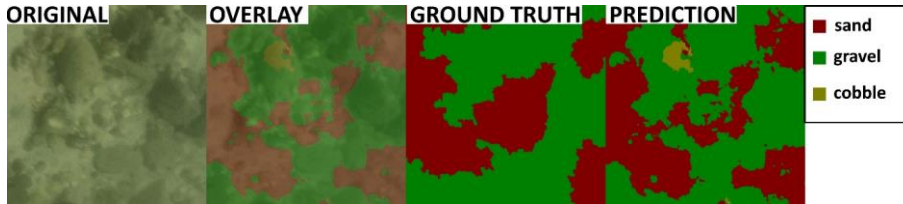
395 indicating the overlap of ground truth area and prediction area, divided by their union (Rahman and Wang, 2016).
 396 This parameter showed a much slighter agreement of 41.46%. Interestingly, there were ~~many~~ cases, where the
 397 model gave better result, than the annotating personnel. While this highlighted the importance of thorough and
 398 precise annotation work, it also showcased that the number of poor annotations was relatively low, so that the
 399 algorithm could still carry out correct learning process and later detections, while not being severely affected by
 400 the mistake of the training personnel. The first row of Figure Fig. 75. showcases antwo examples for this: -i) the
 401 correct appearance of cobble (yellow) in the prediction, even though the user (ground truth) did not define it during
 402 the training; -ii) correctly sensing gravel in the middle of the image, contrary to a whole sand (red) patch in the
 403 ground truth image. As a matter of fact, these positive errors also decrease the IoU evaluation parameter, even
 404 though they increase the performance of the AI on the long term. Hence, this shows that pure mathematical
 405 evaluation may not describe the model performance entirely. Considering that others also reported similar
 406 experience with Deep Learning (Lu et al., 2018) and the fact that 40% and 50% are generally accepted IoU
 407 threshold values (Yang et al., 2018; Cheng et al., 2018; Padilla et al., 2020), we considered the 41.46% acceptable.
 408 The general quality of our underwater images may have also played a role in lowering the IoU result.



409 Figure 65: Example comparisons of ground truth (taught pattern, 3rd column) and AI predicted (learnt pattern, 4th
 410 column) sediment classes from the training videos showing satisfactory results. The 1st column shows raw images, while
 412 the 2nd column overlays the result of the AI detection on the raw image for better visual context.

413
 414
 415

- Formatted: Superscript
- Formatted: Superscript
- Formatted: Superscript
- Formatted: Superscript
- Formatted: Font: (Default) Arial, Not Bold, Italic
- Formatted: Normal, Left



416
417 **Figure 7: Example comparison of ground truth (taught) and AI predicted (learnt) sediment classes from the training,**
418 **in case of training personnel mistake during the annotation.**

Formatted: Normal

Formatted: Font: (Default) Arial, Not Bold, Italic

419 **4.2 Intercomparison of methods**

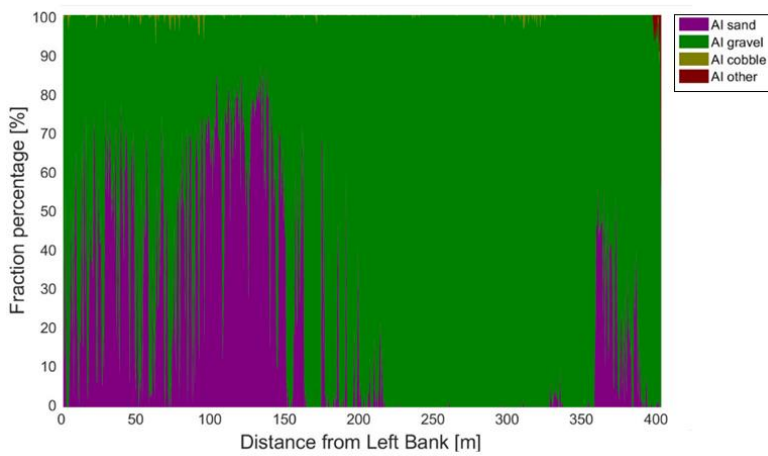
420 In each masked image, the occurring percentage of the given class (i.e., the percentage of the pixels belonging to
421 that class/colour mask, compared to the total number of pixels in the image) was calculated and used as the fraction
422 percentage in that given sampling point. These sediment classes reconstructed by the AI were then compared to
423 three alternative results: i) visual estimation, ii) GSD resulted from conventional grab sampling, iii) wavelet-based
424 image-processing. In the followings, results from two cross-sections will be shown, one from Site A, the video
425 used for the training, and one from Site B, being new for the AI. An averaging window of 15 m was applied on
426 each cross-sectional AI result to smoothen and despiked the dataset.

427
428 In [FigureFig. 86](#), the path of the vessel can be seen in Section K, at Site A. The path was coloured based on the
429 visual evaluation of the riverbed images. The different colours represent the dominant sediment type seen at the
430 given point of the bed. The locations of the physical bed material samplings are also shown (see yellow markers).
431 [Fig. 9 presents the raw \(i.e., before moving-average\) results of the AI detection of each analysed image along](#)
432 [Section K. It can be seen that currentlyCurrently, our approach is sensitive and large spikes, differences can occur](#)
433 [in the AI detection between consecutive, slightly displaced video frames. Due to this, and the fact that there is](#)
434 [uncertainty in the coordinates of the underwater photos and their corresponding physical samples, it is not](#)
435 [recommended to carry out comparisons by selecting certain image and its AI detection. Instead, in this](#)
436 [manuscriptwe applied a moving average-based smoothing for each raw, cross-sectional AI detection, a moving](#)
437 [average-based smoothing was applied, with a window-size corresponding to 15 m. These moving-averages are](#)
438 [the ones being compared later in the sampling points to the physical sampling and the wavelet method. FDespite](#)
439 [this, for the sake of visual supplementationillustration purposes, we provided the raw AI detections of all the](#)
440 [sampling point images, even though their result may not be representative of their corresponding moving-average](#)
441 [values. FigureFig. 107 shows the cross-sectional visual classification compared to the AI-detected sediment](#)
442 [fractions in percentage after applying moving-average \(i.e., the smoothed version of Fig. 9\).](#)



444
 445 Figure 86: The path of the vessel and camera in Section K, Site A. The polyline is coloured based on the sediment
 446 features seen during visual evaluation of the video. Yellow markers are the locations of physical bed material samplings.
 447 (Map created with Google Earth Pro)

448



449
 450 Figure 9: The sediment fraction percentage results of every image, analysed by the AI along Section K. While the trends
 451 are apparent, the sensitivity of the method at its current state can be observed. AI result before applying moving-
 452 averaging.

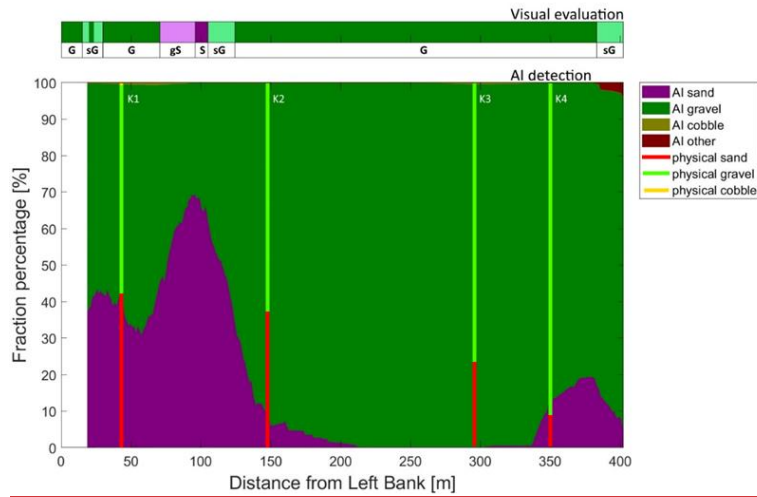
453

Formatted: Centred, Space After: 0 pt

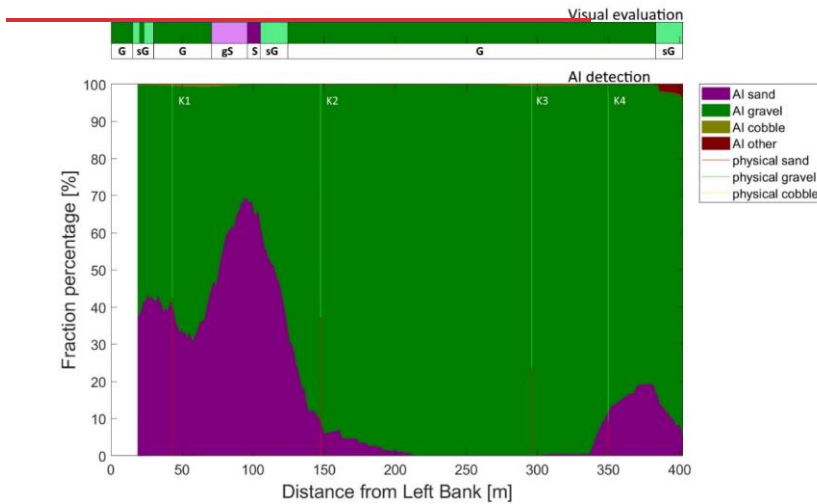
Formatted: Font: (Default) Arial, Not Bold, Italic

Formatted: Normal, Centred

454



455



456

457

458

459

460

Figure 107: Section K. The visual evaluation of the dominant sediment features in the video (top) compared to sediment fraction percentage, recognised by the AI (bottom). AI result after applying moving-averaging. The visual evaluation included four classes: gravel – G, sandy gravel – sG, gravelly sand – gS, sand – S. The fractions of the physical samples are shown as verticals. The fractions from the physical samples are also shown (verticals).

461

462

463

464

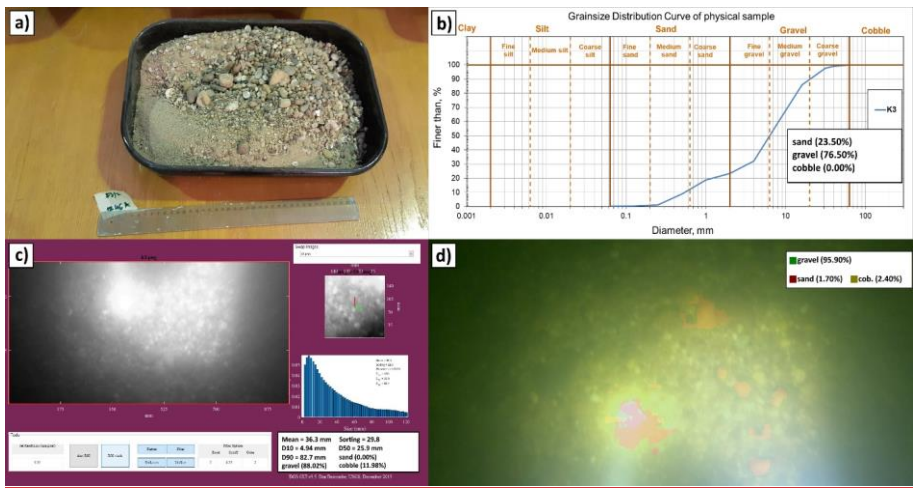
465

466

Comparing the two figures, the AI result shows a satisfactory match with the human evaluation. For example, around 100 m from the left bank, between K1 and K2 sampling points, the AI peaks with around 70% sand and 30% gravel correctly. Furthermore, on the two sides of this peak a steep transition to gravel and decreasing sand occurs, similarly to the eye observation, marked as sandy gravel and gravelly sand. Mixed sediment zones were also correctly identified by the AI at both riverbanks.

467 Next, the AI estimated sediment classes were compared with both the physical samples and the wavelet method
 468 at each sampling locations (Fig. 8). The images of the bed from the sampling points are in shown in Figure 9. As
 469 for the AI results, a moving average-based smoothing was applied in the 15 m vicinity of the sampling locations.
 470 Overall, the AI based classification agrees well with the physical samples, however, at sample K3 the ~20% sand
 471 content was neither reconstructed by the AI, nor could be observed by eye (see Fig. 9). Considering that the gravel
 472 dominates the bed sediments, the absence of sand fraction in the AI results might be explained with the difference
 473 between the surface GSD and subsurface GSD. While both the AI and the eye observation-based assessment focus
 474 on the bed surface, the physical sampling represents a thicker layer, including the subsurface layer, too. Indeed,
 475 the so-called bed armouring phenomenon, taking place in the vicinity of the thalweg in mixed-bed rivers, leads to
 476 coarser surface grains and finer subsurface grains (see e.g., Wilcock, 2005). This may also explain the case of K2
 477 as it was located closer to the thalweg.
 478 Fig. 11. presents an image of the collected physical sample in K3 together with its sieving result. It also compares
 479 these to the as well as the underwater image of the riverbed surface in K3, and the results of the two different
 480 image processing methods. It can be seen that bed armouring is indeed present in the sampling point as the
 481 finer sand fraction cannot be observed on the riverbed surface, yet they appear in the collected bed material
 482 sample. In Fig. 12., supportive images of bed armouring are provided, taken during our surveys in the Upper
 483 section of the Hungarian Danube. We broke the surface armour to showcase the presence of the underlying finer
 484 fractions.

Formatted: Keep with next



486
 487 **Figure 11: Bed armour in sampling point K3. The measured percentages of fractions are also presented, respectively.**
 488 **a) Image of the collected physical sample, containing both sand and gravel fractions. b) GSD curve of the physical**
 489 **sample, produced with sieving analysis. c) Wavelet analysis result of the image, taken in the sampling point. d) AI**
 490 **detection result in the sampling point.**

491



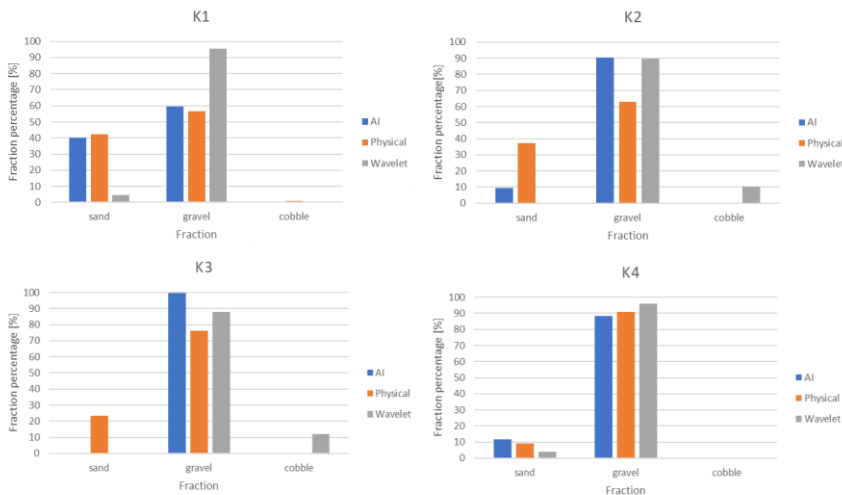
492

493 **Figure 12: Images of bed armoring, taken during our surveys in the Upper section of the Hungarian Danube.**

494 As for the wavelet analysis-based imagery technique, an overall slight overestimation of the coarse particles can be observed, and the sand classes are, in fact, not reconstructed correctly. This finding agrees well with the field
 495 experiences of Ermilov et al. (2020), where the authors indicated the strong sensitivity of the wavelet technique
 496 on the image resolution, and showed that to detect a grain, the diameter must be at least three times larger than
 497 the pixel. In this survey, the camera was indeed closer to the riverbed at sampling points K1 and K4 and the
 498 wavelet algorithm was able to detect coarse sand, but finer sand was neglected yielding the lower percentages,
 499 seen in Fig. 13ure 8.

500

501



502

503 **Figure 138: Comparison of sediment fraction % at the sampling locations from the moving-averaged AI detection,**

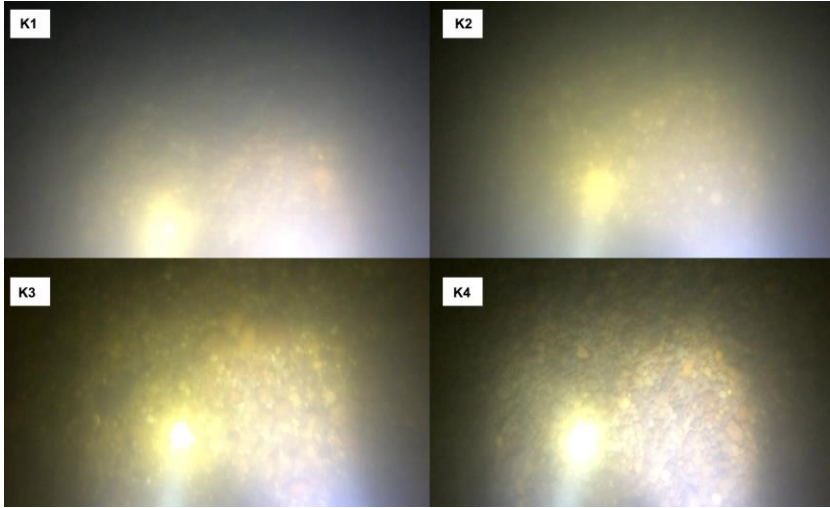
504 **conventional sieving and the wavelet-based image processing method. Section K.**

Formatted: Centred

Formatted: Font: 9 pt, Bold

Formatted: Caption, Line spacing: single

505

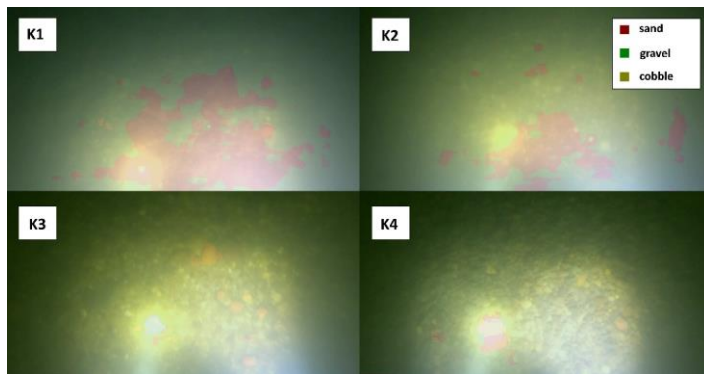


Formatted: Font: (Default) Arial, Not Bold, Italic

Formatted: Normal, Left

506
507

Figure 149: Riverbed video images at the sampling points in Section K.



Formatted: Centred

508

509

Figure 15: Riverbed video images overlapped with their raw, AI detection result, at the sampling points in Section K.

Formatted: Font: Bold

Formatted: Caption, Justified, Line spacing: single

510

At site B (Fig. 169) the river morphology is more complex compared to Site A as a groyne field is located along the left bank (see again Fig. 3). As such, the low flow regions between the groynes yields the, deposition of fine sediments, and much coarser bed composition in the narrowed main stream. Even though no images containing only fine sediments were applied in the training phase of the AI algorithm, the model still managed to successfully distinguish these zones. The fine sediments in the deposition zone at the left bank was adequately estimated and showed a good match with the visual evaluation for the whole cross-section (see Fig. 4+17).

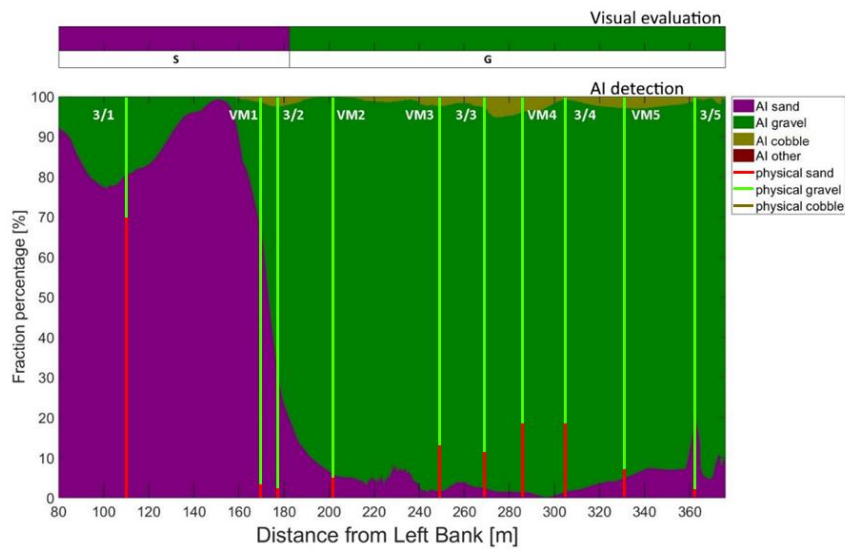
515

516

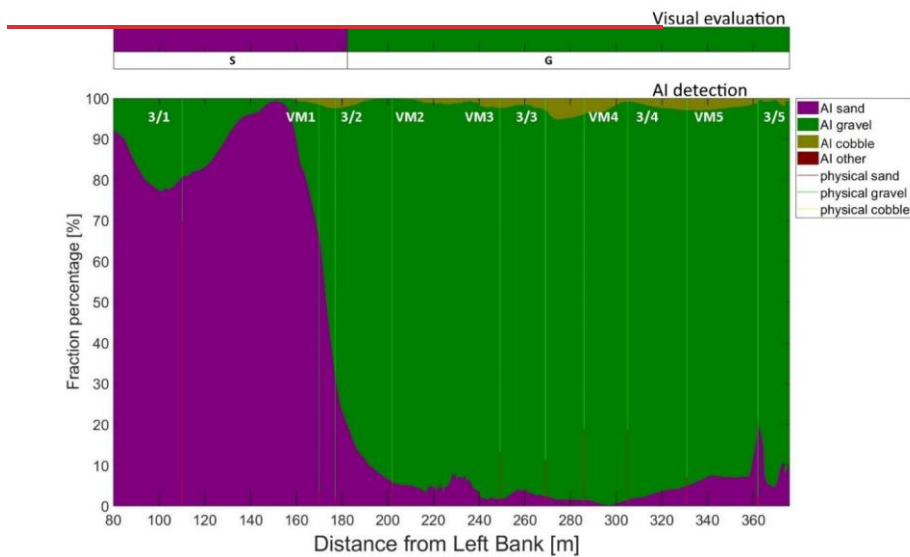


517
 518 **Figure 1016:** The path of the vessel and camera in Section VM, Site B. The polyline is coloured based on the sediment
 519 seen during visual evaluation of the video. Yellow markers are the locations of physical bed material samplings. (Map
 520 created with Google Earth Pro)

521



522



523

524

525

526

Figure 174: Sediment fraction percentages in Section VM, recognised by the AI. The visual evaluation included two classes: gravel – G, sand – S). The fractions of the physical samples are shown as verticals. The fractions from the conventional, point samples are also shown (verticals).

527

528

529

530

531

When comparing the AI results with the physical samples, the match is acceptable for most of the samples, such as 3/1, VM2, VM3, 3/3, VM4, 3/4, VM5, respectively, with a highest difference of 10%. The significant disagreements arose at sampling points VM1 and 3/2. Indeed, these points are located around the border of the sediment deposition zone, showing steeply decreasing amount of sand moving away from the left bank (see

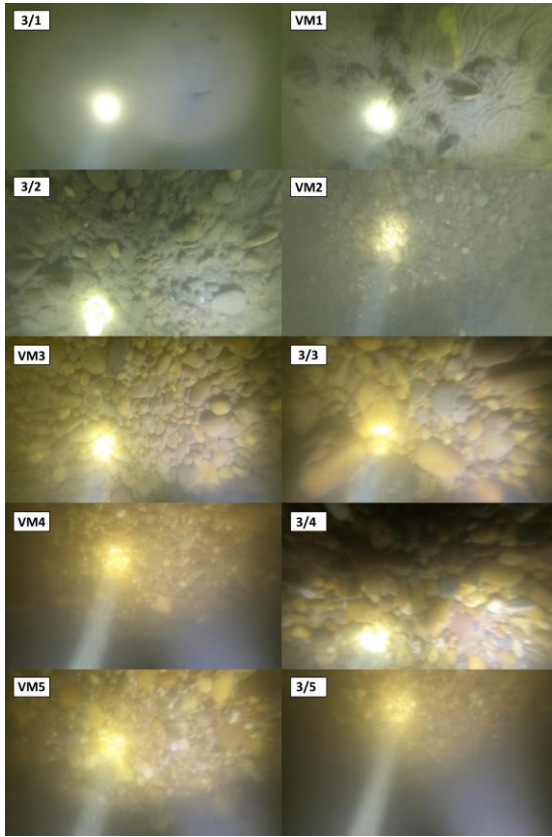
532 the variation from point 3/1 towards 3/2 in Fig. 182). This trend is successfully calculated by the AI algorithm,
533 but the physical samples for points VM1 and 3/2 show strong gravel dominance with negligible amount of sand
534 (see Fig. 1319). Resembling the findings at the other study site, this difference can likely be explained with the
535 disturbed physical samples, which contain the sediments of the subsurface layer, too. In this case, however, the
536 fine sediment layer is accumulated on the gravel particles. It is also worth noting that the physical samples are
537 analysed by weighing the different sediment size classes, resulting in weightvolumetric distribution. On the other
538 hand, the imagery methods provide surface distributions, hence having a thin layer of fine sediments on the top
539 can strongly bias the resulted composition (Bunte and Abt, 2001; Sime and Ferguson, 2003; Rubin et al., 2007).

540 In Fig. 20/a, the grainsize frequency diagram (blue) showcases how the wavelet method incorrectly detected a
541 gravel and a larger cobble mode and it did not manage to identify sand. Again, this was due to not achieving the
542 sufficient image resolution required by the wavelet method. Fig. 20/b on the other hand presents the AI detection
543 for the very same image, with satisfactory results. The algorithm managed to segment the gravels and the sand
544 patches.

545 At sampling point 3/5 a weaker, but still satisfactory agreement was found. Here, the AI indicated 20% sand in
546 contrast with the physical samples. Analysis of the raw videos may indicate that the suspended sediment
547 concentration was higher in this region and the transported fine particles frequently became visible passing
548 through the light beams, eventually causing disturbance in the AI analysis. Another issue in the AI algorithm was
549 associated with the illumination. As a matter of fact, a part of the images was sometimes overexposed, and the too
550 high light intensity biased the results. Using a diving light with small beam divergence proved counterproductive.
551 The high intensity, focused light occasionally caused overexposed zones (white pixels) in the bed image,
552 misleading the AI and resulting in detecting incorrect classes there. The use of wide beam divergence lamps is
553 recommended instead, with uniform light. Examples for these problems are illustrated in FigureFig. 2214 (a:
554 overexposure, b: moving suspended sediment).

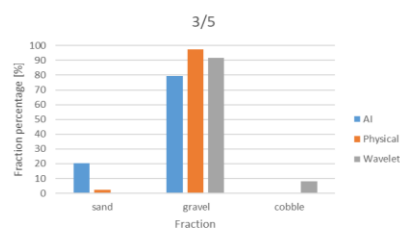
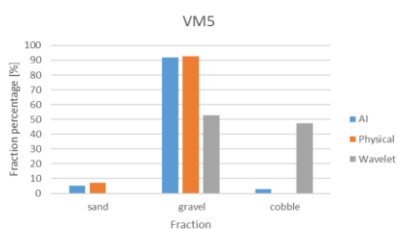
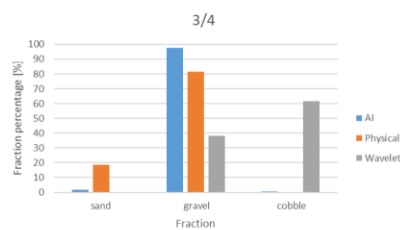
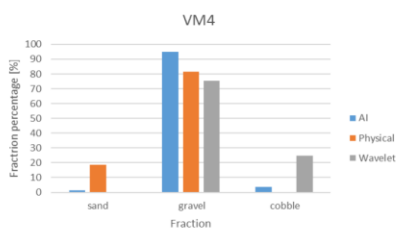
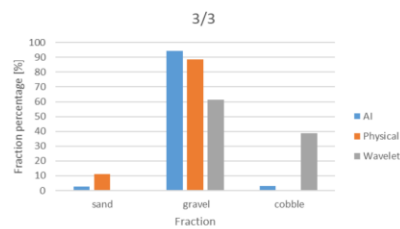
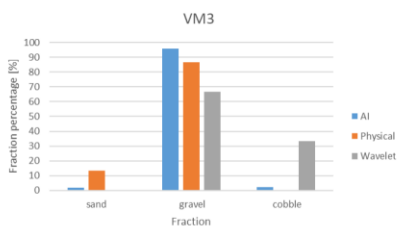
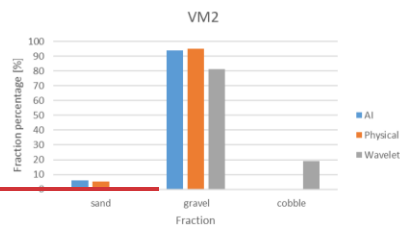
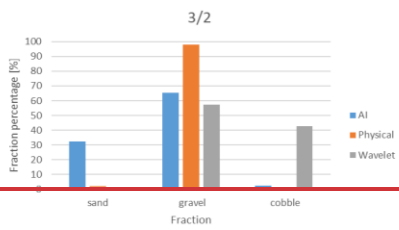
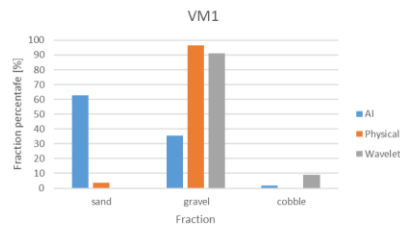
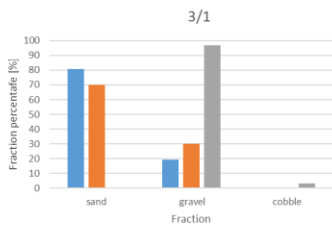
555
556 ~~The resolution was again not sufficient for the wavelet method, and it estimated gravel and cobble regions.~~
557 ~~Contrary to the previous example, it did not manage to identify coarse sand.~~

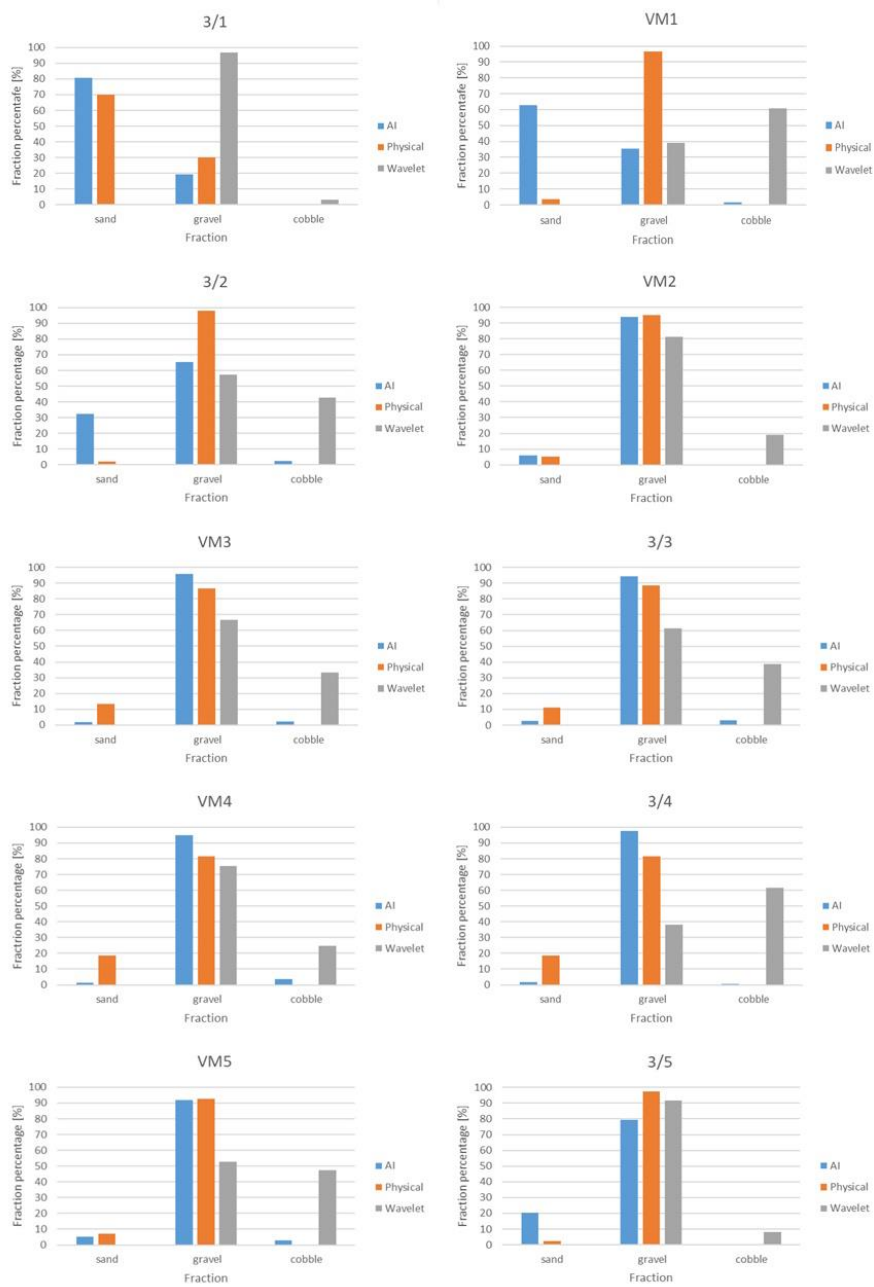
558
559



560
561

Figure 182: ~~River bed~~Riverbed video images at the sampling points in Section VM.





563
564
565

Figure 1913: Comparison of sediment fraction % at the sampling locations from the moving-averaged AI detection, conventional sieving and the wavelet-based image processing method. Section VM.

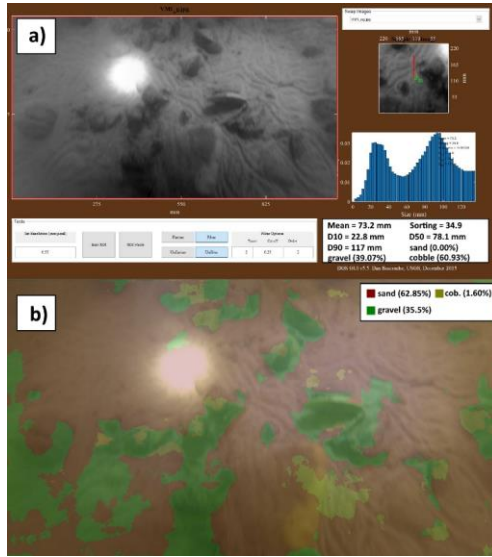
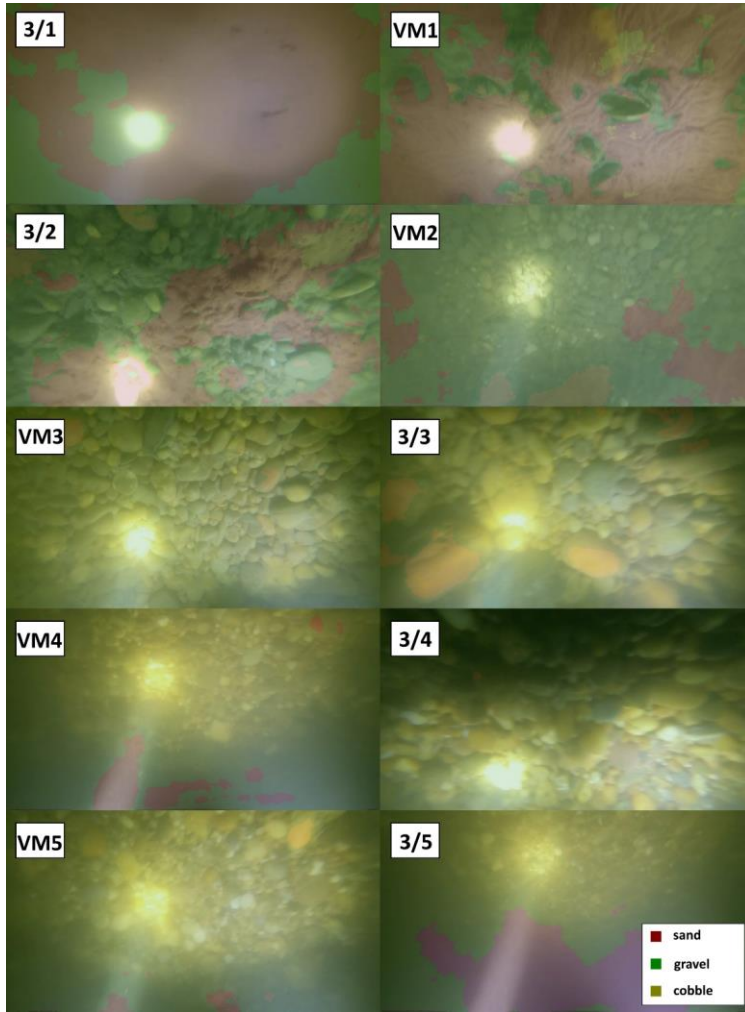


Figure 20: a) Wavelet analysis result of the underwater image in VM1. b) AI detection result of the same image.

Formatted: Font: (Default) Arial, Not Bold, Italic

Formatted: Normal, Left



569
570
571
572

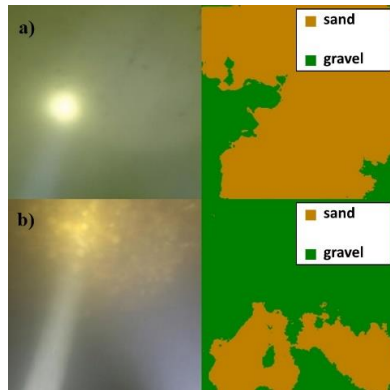
Figure 21: Riverbed video images overlapped with their raw, AI detection result, at the sampling points in Section VM.

Formatted: Centred

Formatted: Centred

Formatted: Font: (Default) Arial, Not Bold, Italic

Formatted: Normal, Left



573
574
575 Figure 2214: The effect of strong diving light on the AI algorithm in: a) purely sand covered zone and b) darker zone with higher SSC. The original images are on the left, while the AI detections can be found on the right.

Formatted: Tab stops: 2,25 cm, Left

576
577 Results of the other measurements can be found in the Appendix. FigureFig. A2, B2 and C2 show that the trend
578 of riverbed composition from the visual evaluation is well-captured by the AI in the other cross-sections of the
579 study as well (see sampling points F/3, F/4, 1/1, 1/2 1/3, respectively). The resolution limit of the wavelet approach
580 was further noticeable (see FigureFig. A3, B3 and C3) as it was not able to detect sand, similarly to the sampling
581 points presented earlier. In Section A, traces of possible bed armouring were found as neither the eye observation
582 nor the AI detected sand class in the images (see FigureFig. B4) of F/1 and F/2, even though the physical samples
583 contained this fraction. In sampling point 1/4, the AI correctly detected the mixing of sand and gravel, but the
584 physical sample showed the dominance of sand rather than the gravel fraction (see FigureFig. C3). The possible
585 explanation behind these differences resembles what was the case for the K3 sampling point, introduced earlier:
586 there was an additional finer fraction in the subsurface layer, hidden from the camera. Based on the results
587 presented in this ~~paper~~manuscript, it could be established that the AI manages to recognise the main features of
588 the riverbed material composition from underwater videos with satisfactory accuracy.

589 4.3 Implementation challenges

590 The power supply for the entire imaging infrastructure, i.e., for the camera, the diving lights and lasers, was
591 ensured by batteries. However, due to the low temperature at the river bottom, the battery level decreased
592 extremely fast, compared to normal circumstances. Providing the power supply directly from the motorboat
593 engines can overcome this issue. To keep the camera in the adequate height also caused difficulties, since getting
594 too close to the bed can harm the devices, lifting too high, on the other hand, will result in poor image quality.
595 The measured instantaneous ADCP flow depth data was used therefore to keep the bed in camera sight, while
596 maintaining proper boat velocity to avoid blurry images. ~~We found that a 0.2-0.45 m/s vessel speed with 60 fps~~
597 ~~recording frequency was ideal to retrieve satisfactory images in a range of 0.4-1.6 m camera-bed distances. This~~
598 ~~meant approximately 15 minutes long measurements per transects. Higher vessel speed caused blurred images.~~
599 Choosing a higher recording frequency, however, can be beneficial and alter this limitation, when provided. Lower
600 velocities could not be maintained as the river would have moved the vessel out of the section. An alternative
601 solution can be to move on longitudinal (streamline) paths instead of transects. This would allow for lower vessel
602 speed. This would increase the time of the measurement, which in-itself could still could be profitable if the images

603 are of higher quality. However, the conventional way for river bathymetry surveys is to move on transversal,
604 cross-sectional paths, due to the river bathymetry having a lower spatial variation along streamlines, compared to
605 the changes that occur in the transversal direction (Benjankar et al., 2015; Kinsman, 2015). As such, it may require
606 carrying out a relatively dense set of longitudinal paths to gain proper information, further increasing the necessary
607 amount of time demand. Thus, for this alternative, higher attention needs to be paid towards choosing these paths
608 and the interpolation method. Using a diving light with small beam divergence also proved counterproductive.
609 The high intensity, focused light occasionally caused overexposed zones (white pixels) in the bed image,
610 misleading the AI and resulting in detecting incorrect classes there. The use of wide beam divergence lamps is
611 recommended instead, with uniform light. Further attention needs to be paid to the reel and its cable during the
612 crossing when the equipment is on the upstream side of the boat. If the flow velocities are relatively high
613 (compared to the total submerged weight of the underwater equipment), the cable can be pressed against the
614 vessel body due to the force from the flow itself, causing the reel cable to jump to the side and leave its guide.
615 This results in the equipment falling to the riverbed and the measurement has to be stopped to reinstall the
616 cable. Another challenge can be the influence of drag force on the measurement setup. In our case, even though
617 the main body itself was a streamlined weight, equipping the other tools on it turned the setup geometry irregular.
618 Additionally, we found that our setup was a bit nose-heavy. Moreover, our setup proved to be a bit nose-heavy as
619 well. Due to this, and the drag force combined, the camera tilted forward during the measurements. As a result,
620 the lower parts of the raw images were sometimes too dark, as the camera was looking over the riverbed, and not
621 at the lit part of the bed. Examples for this could be seen in Fig. 18 (VM4, VM5, 3/5). Hence, in this manuscript
622 we decided to crop out the lower 25% of all raw images generally, before processing them to avoid this element
623 of uncertainty. On the long term however, this effect could be reduced by building a streamlined container (e.g.,
624 3D-printed body, or a body similar to unmanned underwater vehicles') with slots in it for each device, and also
625 by improving the weight distribution. Furthermore, we hypothesize that by using lasers (as originally planned in
626 this study) during the measurements, the known structure (i.e., the position and distances) of the laser points when
627 the setup is perpendicular to the bed, can help to orthorectify the images. This will decrease the effect of occasional
628 tilting when one wishes to carry out size analysis on the images. In our case, we presented how the wavelet method
629 had inherently bigger issues (i.e., image resolution limit), which could not be caused by the camera tilting since
630 those would be in a significantly lower magnitude of error.

631
632 As for the training of the AI algorithm with the underwater images, the illumination is indeed a more crucial
633 aspect, compared to normal imagery methods. In many cases only the centre areas of the images were clearly
634 visible, whereas the remaining parts were rather dark and shady. Determining the boundaries between distinct
635 sediment classes for these images was challenging even for experienced eyes. This quality issue certainly
636 generated some incorrect annotations. To overcome this issue, manually varying the white balance thus enhancing
637 the visibility of the sediment could improve the training to some extent. It is worth noting that when Deep Learning
638 methods are to be used, most of the problems arise from the data side (Yu et al., 2007), whereas issues related to
639 the applied algorithms and hardware are rare. This is because data is more important from an accuracy perspective
640 than the actual technical infrastructure (Chen et al., 2020). The time demand of image annotation (data
641 preparation) is relatively high, i.e., an untrained person could analyse roughly 10 images per hour. On the other
642 hand, as introduced earlier, a great advantage of using AI is the capability of improving the quality of training

643 itself, often yielding better agreement with reality, compared to the manual annotation. Similar results have been
644 reported by Lu et al., (2018). This at the same time proves that [with the introduced approach](#), there is no need for
645 very precise manual training, thus a fast and effective training process can eventually be achieved.

646
647 The validation of the Deep Learning algorithm is far from straightforward. In this study, four approaches were
648 adapted, i.e., a mathematical approach, and comparison with three other measurement methods, respectively. The
649 mathematical approach was based on calculating pixel accuracy and the Intersection-over-union parameter, as it
650 is usually done in case of Deep Learning methods to describe their efficiency (e.g. Rahman and Wang, 2016).
651 However, the latter parameter was shown to be decreased even when the model improved. Consequently, using
652 only the mathematical evaluation in this study could not describe adequately the model performance. Hence, the
653 results were compared to those of three other methods: i) visual evaluation of the image series, ii) a wavelet-based
654 image-processing method (using the method of Buscombe, 2013) and iii) riverbed composition data from physical
655 samples. Considering the features of the applied methods, the first one, i.e., the visual observation, is expected to
656 be the most suitable for the model validation. Indeed, when assessing the bed surface composition by eye, the
657 same patterns are sought, i.e., both methods focus on the uppermost sediment layer. On the other hand, the physical
658 sampling procedure inherently represents subsurface sediment layers, leading to different grain size distributions
659 in many cases. For instance, as shown above, if bed armour develops in the riverbed and the sampler breaks-up
660 this layer, the resulted sample can contain the finer particles from the subsurface layer. On the contrary, in zones
661 where a fine sediment layer is deposited on coarse grains, i.e., a sand layer on the top of a gravel bed, the physical
662 samples represent the coarse material too, moreover, considering that the sieving provides [weight-volumetric](#)
663 distribution this sort of bias will even enhance the proportion of the coarse particles. Attempts were made to
664 involve a third, wavelet-based method for model validation. However, this method failed when finer particles,
665 i.e., sand, characterized the bed. This is an inherent limitation of these type of methods, as [discussed earlier, shown](#)
666 [already by Buscombe and Masselink \(2008\), Cheng \(2015\) or Ermilov et al \(2020\)](#), as the image resolution, i.e.
667 the pixel size, is simply not fine enough to reconstruct the small grain diameters in the range below fine gravel.

668
669 As it is known, the ML and DL models can learn unknown relationships in datasets, but unwanted biases as well.
670 With our current dataset, in our opinion, these biases would be the darker tones of visible grain texture and the
671 lack of larger grain sizes. This way our model in its current state is only applicable effectively in the chosen study
672 site, until the dataset is not expanded with additional images from other rivers or regions. However, the purpose
673 of the [papermanuscript](#) was to introduce the methodology itself and its potential in general and not to create a
674 universal algorithm.

675 4.4 Novelty and future work

676 The introduced image-based Deep Learning algorithm offers novel features in the field of sedimentation
677 engineering. First, to the authors' knowledge, underwater images of the bed of a large river have not yet been
678 analysed by AI. Second, the herein introduced method enables [continuous-extensive](#) (and [still relatively](#) quick)
679 mapping of the riverbed, in contrast to most of the earlier approaches, where only [several](#) points or shorter sections
680 were assessed with imagery methods. Third, the method is much faster compared to conventional samplings or
681 non-AI based image-processing techniques. The field survey of a 400 m long transect took ~15 minutes, while

682 the AI analysis took 4 minutes (approx. 7 image/s). The speed range of 0.2-0.45 m/s of the measurement vessel
683 and the 15 minutes per transect complies with the operating protocol of general ADCP surveys on rivers (e.g., RD
684 Instruments, 1999; Simpson, 2002; Mueller and Wagner, 2013). Hence, the developed image-based measurement
685 can be carried out together with the conventional boat-mounted ADCP measurements, further highlighting its time
686 efficiency. Indeed, the method is a great alternative approach for assessing riverbed material on-the-go, in
687 underwater circumstances. As an ~~extensive-continuous~~ and quick mapping tool, it can support other types of bed
688 material samplings in choosing the sampling locations and their optimal number. Furthermore, it can be used for
689 quickly detecting areas of sedimentation and their extent, as it was shown in Ch. 4.2. (~~FigureFig.~~ 174). This way,
690 it may support decisions regarding the maintenance of the channel or the bank-infiltrated drinking water
691 production (detecting colmatation and colmated zones). Fourth, a novel approach was used for the imaging and
692 model training. As the camera-bed distance were constantly changing, the mm/pixel ratio also varied. Hence, no
693 scale was defined for the algorithm beforehand. Earlier Deep Learning methods for sediment analysis all applied
694 fixed camera heights and/or provided scaling for the AI. It should be noted that these were airborne measurements,
695 mapping the dry zone of the rivers. In an underwater manner, it is extremely challenging to keep a fixed, constant
696 camera height due to the spatially varying riverbed elevations. Hence, it is of major importance that this
697 ~~papermanuscript~~ introduces a methodology and a Deep Learning algorithm which neglect the need for scaling.
698 This way, the method is faster and easier to build, but also simpler to use. Of course, as a trade-off, the method,
699 as of now, cannot reconstruct detailed grainsize distributions. Indeed, the purpose was rather to provide a uniquely
700 fast bed material mapping tool, additionally with a much denser spatial resolution than the conventional methods,
701 saving up significant resources.

702
703 Originally, beside the three main sediment grain classes introduced in the ~~papermanuscript~~ (sand, gravel, cobble),
704 others were also defined during annotation (e.g., bedrock, clams), but due to class imbalance (i.e., dominance of
705 the three sediment classes), these were not adapted successfully. There is a good potential in improving the method
706 through transfer learning (see Zamir et al., 2018) using broader dataset, involving other sediment types. Another
707 possible way to counter imbalance is the use of so-called weighted cross entropy (see Lu et al., 2019) on the
708 current dataset, which will also be investigated in our case.

709
710 Since the introduced method offers a quick way to provide ~~extensive,~~ spatially ~~dense-continuous~~ bed material
711 information of its composition, it may be used to boost the training dataset of predictive, ensemble bagging-based
712 Machine Learning techniques (e.g., Ren et al., 2020) and improve their accuracy. Furthermore, the method can
713 support the implementation of other imagery techniques. For instance, using one of the training videos of this
714 study the authors managed to reconstruct the grain-scale 3D model of a riverbed section with the Structure-from-
715 Motion technique (Ermilov et al., 2020), enabling the quantitative estimation of surface roughness. Underwater
716 field cameras can also be used for monitoring and estimating bedload transport rate (Ermilov et al., 2022) by
717 adapting LS-PIV and the Statistical Background Model approach. This latter videography technique may also be
718 used with moving cameras (e.g., Hayman and Ekhlund, 2003), which enables its adaptation into our method by
719 e.g., detecting bedload movement in the cross-section.

720 5 Conclusion

721 A novel, artificial intelligence-based riverbed sediment analysis method has been introduced in this
722 [papermanuscript](#), which uses underwater images to reconstruct the spatial variation of the characteristic sediment
723 classes. The method was trained and validated with a reasonably high number (~15000) of images, collected in a
724 large river, in the Hungarian section of the Danube. The main novelties of the developed Deep Learning based
725 procedure are the followings: i) underwater images are used, ii) the method enables ~~continuous~~ mapping of the
726 riverbed along the measurement vessel's route [with very dense spatial allocation](#), iii) cost-efficient, iv) works
727 without scaling, i.e., the distance between the camera and the riverbed can vary. Consequently, in contrast with
728 conventional pointwise bed sediment analysis methods, this technique is robust and capable of providing
729 continuous sediment composition data covering whole river reaches, eventually providing the possibility to set up
730 2D bed material maps. In this way, river reach scale hydromorphological assessments can be supported, where
731 the composition of bed surface is of interest, e.g., when performing habitat studies, parameterising 2D and 3D
732 computational hydrodynamic and morphodynamic models, or assessing the impact of restoration measures.

733 **Financial support.** The first author acknowledges the support of the ÚNKP-21-3 New National Excellence
734 Programme of the Ministry for Innovation and Technology, and the National Research, Development and
735 Innovation Fund, Hungary.

736 **Code availability.** The code written and used in this [papermanuscript](#) is available here: [https://bmeedu-](https://bmeedu-my.sharepoint.com/:f/g/personal/ermilov_alexander_emk_bme_hu/Ejl2neM4AOZGsBkYgKReViEBBzRFRFoYyLlmo6SzTB_qDQ?e=AqqqHI)
737 [my.sharepoint.com/:f/g/personal/ermilov_alexander_emk_bme_hu/Ejl2neM4AOZGsBkYgKReViEBBzRFRFo](https://bmeedu-my.sharepoint.com/:f/g/personal/ermilov_alexander_emk_bme_hu/Ejl2neM4AOZGsBkYgKReViEBBzRFRFoYyLlmo6SzTB_qDQ?e=AqqqHI)
738 [YyLlmo6SzTB_qDQ?e=AqqqHI](https://bmeedu-my.sharepoint.com/:f/g/personal/ermilov_alexander_emk_bme_hu/Ejl2neM4AOZGsBkYgKReViEBBzRFRFoYyLlmo6SzTB_qDQ?e=AqqqHI)

739 **Data availability.** The dataset and results can be accessed using the following link: [https://bmeedu-](https://bmeedu-my.sharepoint.com/:f/g/personal/ermilov_alexander_emk_bme_hu/EhoGx64sP1tFnj8Z1OdMZAsBZWd5gDYzPyodSUDdWFjeiw?e=hKIXjq)
740 [my.sharepoint.com/:f/g/personal/ermilov_alexander_emk_bme_hu/EhoGx64sP1tFnj8Z1OdMZAsBZWd5gDY](https://bmeedu-my.sharepoint.com/:f/g/personal/ermilov_alexander_emk_bme_hu/EhoGx64sP1tFnj8Z1OdMZAsBZWd5gDYzPyodSUDdWFjeiw?e=hKIXjq)
741 [zPyodSUDdWFjeiw?e=hKIXjq](https://bmeedu-my.sharepoint.com/:f/g/personal/ermilov_alexander_emk_bme_hu/EhoGx64sP1tFnj8Z1OdMZAsBZWd5gDYzPyodSUDdWFjeiw?e=hKIXjq)

742 **Author contributions.** GB developed the code and carried out the training process. AAE carried out the
743 fieldwork, evaluated the results, did the laboratory analysis, and collaborated with GB in improving the images.
744 SB oversaw and directed the project, while managing the financial- and equipment background.

745 **Competing interest.** The contact author has declared that none of the authors has any competing interest.

746 **Acknowledgements.** The authors would like to thank our students Dávid Koós, Gergely Tikász, Schrott Márton
747 and our technicians István Galgóczy, István Pozsgai, Károly Tóth and András Rehák for fieldwork support.

748 References

- 749 Adams, J.: Gravel Size Analysis from Photographs. J. Hydraul. Div., 1979, 105, 1247–1255.
750 doi/10.1061/JYCEAJ.0005283, 1979.
751
752 Anglin, D. R., Haeseker, S. L., Skalicky, J. J., Schaller, H., Tiffan, K. F., Hatten, J. R., et al.: Effects of Hydropower
753 Operations on Spawning Habitat, Rearing Habitat, and Standing/Entrapment Mortality of Fall Chinook Salmon
754 in the Hanford Reach of the Columbia River. US Fish and Wildlife Service, final Report. Available at:
755 <https://pubs.er.usgs.gov/publication/70179516>, 2006.

756
757 Baranya, S., Fleit, G., Józsa, J., Szalóky, Z., Tóth, B., Czeglédi, I. and Erős, T.: Habitat mapping of riverine fish
758 by means of hydromorphological tools. *Ecohydrology*, Volume 11, Issue 7 e2009. Available at:
759 <https://doi.org/10.1002/eco.2009> , 2018.
760
761 Barnard, P., Rubin, D., Harney, J. and Mustain, N.: Field test comparison of an autocorrelation technique for
762 determining grain size using a digital beachball camera versus traditional methods. *Sedimentary Geology*, 201(1–
763 2): 180–195., 2007.
764
765 ~~Benjankar, R., Tonina, D., Mckean, J.: One-dimensional and two-dimensional hydrodynamic modelling derived~~
766 ~~flow properties: Impacts on aquatic habitat quality predictions. *Earth Surf. Process. Landf.* 2015. 40. 340–356.~~
767
768 Benkő, G., Baranya, S., Török, T. G., and Molnár, B.: Folyami mederanyag szemösszetételének vizsgálata Mély
769 Tanulás eljárással drónfelvételek alapján (in English: Analysis of composition of ~~river-bedriverbed~~ material with
770 Deep Learning based on drone video footages). *Hidrológiai Közlöny*, 100, 61–69., 2020.
771
772 ~~Bovee, K. D.: A guide to stream habitat analysis using the. *Instream Flow Incremental Methodology. Instream*
773 ~~Flow Information, PaperManuscript no. 12., U.S.D.I. Fish and Wildlife Service, Office of Biological Services.~~
774 ~~FWS/OBS-82/26. 248 pp., 1982.~~
775
776 Breheret, A.: Pixel Annotation Tool. Av. at: <https://github.com/abreheret/PixelAnnotationTool>, 2017.
777
778 Bunte, K. and Abt, S. R.: Sampling Surface and Subsurface Particle-Size Distributions in Wadable Gravel- and
779 Cobble-Bed Streams for Analyses in Sediment Transport, Hydraulics, and Streambed Monitoring; General
780 Technical Report (GTR), U.S. Department of Agriculture, Forest Service, Rocky Mountain Research Station: Fort
781 Collins, CO, USA, 2001.
782
783 ~~Butler, J. B., Lane, S. N. and Chandler, J. H.: Automated extraction of grain size data from gravel surfaces using~~
784 ~~digital image processing. *J. Hydraul. Res.*, 39, 519–529., 2001.~~
785
786 Buscombe, D. and Masselink, G.: Grain size information from the statistical properties of digital images of
787 sediment. *Sedimentology*, 56, 421–438. doi/10.1111/j.1365-3091.2008.00977.x, 2008.
788
789 Buscombe, D.: Transferable wavelet method for grain-size distribution from images of sediment surfaces and thin
790 sections, and other natural granular patterns. *Sedimentology*, 60 1709–1732., 2013.
791
792 Buscombe, D., Grams, P. and Kaplinski, M.: Characterizing riverbed sediment using high-frequency acoustics: 1.
793 Spectral properties of scattering. *Journal of Geophysical Research: Earth Surface*, doi: 10.1002/2014JF003189,
794 119:12, (2674-2691), 2014a.
795
796 Buscombe, D., Grams, P. and Kaplinski, M.: Characterizing riverbed sediment using high-frequency acoustics: 2.
797 Scattering signatures of Colorado ~~River-bedRiverbed~~ sediment in Marble and Grand Canyons. *Journal of*
798 *Geophysical Research: Earth Surface*, doi/full/10.1002/2014JF003191, 119:12, (2674-2691), 2014b.
799
800 Buscombe, D. and Ritchie, A. C.: Landscape Classification with Deep Neural Networks. *Geosciences*, 8, 244.
801 Available at: <https://doi.org/10.3390/geosciences8070244> , 2018.
802
803 Buscombe, D.: SediNet: a configurable deep learning model for mixed qualitative and quantitative optical
804 granulometry optical granulometry. *Earth Surface Processes and Landforms*, 45, 638-651. DOI:
805 10.1002/esp.4760, 2020.
806
807 ~~Butler, J. B., Lane, S. N. and Chandler, J. H.: Automated extraction of grain size data from~~
808 ~~gravel surfaces using digital image processing. *J. Hydraul. Res.* 2001, 39, 519–529. Available at:~~
809 ~~<https://doi.org/10.1080/00221686.2001.9628276>.~~
810
811 ~~Carbonneau, P. E., Lane, S. N and Bergeron, N. E.: Catchment scale mapping of surface grain size in gravel bed~~
812 ~~ivers using airborne digital imagery. *Water Resources Research*, 40(7): W07202., 2004.~~
813~~

814 Chandler, J., Lane, S. N. and Ashmore, P.: Measuring river-bed and flume morphology and parameterising bed
815 roughness with a KODAK DCS460 digital camera. *International Archives of Photogrammetry and Remote*
816 *Sensing*, Vol. XXXIII, Part B7., 2000.

817

818 Chen, C., Zhang, P., Zhang, H., Dai, J., Yi, Y., Zhang, H. and Zhang, Y.: Deep Learning on Computational-
819 Resource-Limited Platforms: A Survey. Volume 2020, Article ID 8454327. Available at:
820 <https://doi.org/10.1155/2020/8454327>, 2020.

821

822 Chen, L., Zhu, Y., Isola, P., Papandreou, G., Schroff, F. and Adam, H.: Encoder-Decoder with Atrous Separable
823 Convolution for Semantic Image Segmentation. *Proceedings of the European conference on computer vision*
824 (ECCV) (pp. 801-818). <https://arxiv.org/abs/1802.02611>, 2018.

825

826 Cheng, D., Li, X., Li, W. H., Lu, C., Li, F., Zhao, H. and Zheng, W. S.: Large-Scale Visible Watermark Detection
827 and Removal with Deep Convolutional Networks. In book: *Pattern Recognition and Computer Vision. First*
828 *Chinese Conference, PRCV, Guangzhou, China, Proceedings, Part III*. DOI: 10.1007/978-3-030-03338-5_3,
829 2018.

830

831 Cheng, Z., and Liu, H.: Digital grain-size analysis based on autocorrelation algorithm. *Sedimentary Geology*, 327,
832 21-31. Available at: <https://doi.org/10.1016/j.sedgeo.2015.07.008>, 2015.

833

834 Chezar, H. and Rubin, D. M.: Underwater Microscope System. United States Patent Office, The United States of
835 America as represented by the Secretary of the Interior, US Patent No. 6,680,795 B2., 2004.

836

837 Church, M. A., McLean, D. G., and Wolcott, J. F.: Sediments transport in Gravel Bed Rivers. Chap.: **River**
838 **BedRiverbed** Gravels: Sampling and Analysis. John Wiley and Sons, New York, 43–88, 1987.

839

840 Delong, M. D. and Brusven, M. A.: Classification and spatial mapping of riparian habitat with applications toward
841 management of streams impacted by nonpoint source pollution. *Environmental Management*, 15:565-571. DOI:
842 10.1007/BF02394745, 1991.

843

844 Detert, M. and Weitbrecht, V.: User guide to gravelometric image analysis by BASEGRAIN. In *Advances in*
845 *Science and Research*; Fukuoka, S., Nakagawa, H., Sumi, T., Zhang, H., Eds.; Taylor and Francis Group: London,
846 UK, 2013; pp. 1789–1795. ISBN 978-1-138-00062-9., 2013.

847

848 Diplas, P.: Sampling Techniques for Gravel Sized Sediments. *Journal of Hydraulic Engineering*. DOI:
849 10.1061/(ASCE)0733-9429(1988)114:5(484), 1988.

850

851 Ermilov, A. A., Baranya, S. and Török, G.T.: Image-Based Bed Material Mapping of a Large River. *Water*, 12,
852 916. Available at: <https://doi.org/10.3390/w12030916>, 2020.

853

854 Ermilov, A. A., Fleit, G., Conevski, S., Guerrero, M., Baranya, S., & Rütger, N.: Bedload transport analysis using
855 image processing techniques. *ACTA GEOPHYSICA*, 1895-6572 1895-7455. [http://doi.org/10.1007/s11600-022-](http://doi.org/10.1007/s11600-022-00791-x)
856 [00791-x](http://doi.org/10.1007/s11600-022-00791-x), 2022.

857

858 Fehr, R.: Einfache Bestimmung der Korngrößenverteilung von Geschiebematerial mit Hilfe der
859 Linienzahlanalyse (In English: Simple detection of grain size distribution of sediment material using line-count
860 analysis). *Schweizer Ing. und Archit.*, 105, 1104–1109., 1987.

861

862 [Ferdowsi, B., Ortiz, C. P., Houssais, M., & Jerolmack, D. J. \(2017\). Riverbed armouring as a granular segregation
863 phenomenon. *Nature Communications* 2017 8:1, 8\(1\), 1–10. <https://doi.org/10.1038/s41467-017-01681-3>](https://doi.org/10.1038/s41467-017-01681-3)

864

865 Fetzner, J., Holzner, M., Plötze, M. and Furrer, G.: Clogging of an Alpine streambed by silt-sized particles –
866 Insights from laboratory and field experiments. *Water Research*, Volume 126, Pages 60-69.
867 <https://doi.org/10.1016/j.watres.2017.09.015>, 2017.

868

869 Geist, D. R., Jones, J., Murray, C. J. and Dauble, D. D.: Suitability criteria analyzed at the spatial scale of redd
870 clusters improved estimates of fall chinook salmon (*Oncorhynchus tshawytscha*) spawning habitat use in the
871 Hanford Reach, Columbia River. *Canadian Journal of Fisheries and Aquatic Sciences*, 57: 1636-1646., 2000.

872

Formatted: Justified, Line spacing: single

Formatted: Justified, Indent: Left: 0,85 cm

873 Gilcher, M. and Udelhoven, T.: Field Geometry and the Spatial and Temporal Generalization of Crop
874 Classification Algorithms—A Randomized Approach to Compare Pixel Based and Convolution Based Methods.
875 Remote Sens., 13, 775., 2021.

876
877 GOPRO Hero 4 Silver: User Manual. Available at: [https://gopro.com/content/dam/help/hero4-](https://gopro.com/content/dam/help/hero4-silver/manuals/UM_H4Silver_ENG_REVA_WEB.pdf)
878 [silver/manuals/UM_H4Silver_ENG_REVA_WEB.pdf](https://gopro.com/content/dam/help/hero4-silver/manuals/UM_H4Silver_ENG_REVA_WEB.pdf), 2014.

879
880 GOPRO Hero 7 Black: User Manual. Available at: [https://gopro.com/content/dam/help/hero7-](https://gopro.com/content/dam/help/hero7-black/manuals/HERO7Black_UM_ENG_REVA.pdf)
881 [black/manuals/HERO7Black_UM_ENG_REVA.pdf](https://gopro.com/content/dam/help/hero7-black/manuals/HERO7Black_UM_ENG_REVA.pdf), 2018.

882
883 Graham, D. J., Reid, I. and Rice, S. P.: Automated sizing of coarse-grained sediments: image-processing
884 procedures. Mathematical Geology, 37, 1–28. <https://doi.org/10.1007/s11004-005-8745-x>, 2005.

885
886 Graham, D. J. Rollet, A.J., Piégay, H. and Rice, S. P.: Maximizing the accuracy of image-based surface sediment
887 sampling techniques. Water Resour. Res., 46, W02508. [https://doi.org/](https://doi.org/10.1029/2008WR006940)
888 [10.1029/2008WR006940](https://doi.org/10.1029/2008WR006940), 2010.

889
890 Grams, P. E., Topping, D. J., Schmidt, J. C., Hazel, J. E. and Kaplinski, M.: Linking morphody-namic response
891 with sediment mass balance on the Colorado River in Marble Canyon: Issues of scale, geomorphic setting, and
892 sampling design, J. Geophys. Res. Earth Surf., 118, 361–381, doi:10.1002/jgrf.20050., 2013.

893
894 Guerit, L., Barrier, L., Liu, Y., Narteau, C., Lajeunesse, E., Gayer, E., Métivier, F.: Uniform grain-size distribution
895 in the active layer of a shallow, gravel-bedded, braided river (the Urumqi River, China) and implications for paleo-
896 hydrology. Earth Surface Dynamics. 6. 1011-1021. DOI: 10.5194/esurf-6-1011-2018., 2018.

897
898 ~~Guerrero, M. and Lamberti, A.: Flow field and morphology mapping using ADCP and multibeam techniques:
899 Survey in the Po River. J. Hydraul. Eng., 137, 1576–1587, doi:10.1061/
900 (ASCE)HY.1943-7900.0000464., 2011.~~

901
902 Guerrero, M., Rütther, N., Szupiany, R., Haun, S., Baranya, S. and Latosinski, F.: The Acoustic Properties of
903 Suspended Sediment in Large Rivers: Consequences on ADCP Methods Applicability. Water, 8, 13;
904 doi:10.3390/w8010013, 2016.

905
906 Haddadchi, A., Booker, D.J. and Measures, R.J.: Predicting ~~river bed~~ substrate cover proportions across
907 New Zealand. Catena, Volume 163, pp. 130-146. Available at: <https://doi.org/10.1016/j.catena.2017.12.014>,
908 2018.

909
910 Hayman, E., Eklundh, J.: Statistical Background Subtraction for a Mobile Observer. Proceedings of the Ninth
911 IEEE International Conference on Computer Vision (ICCV 2003) 2-Volume Set 0–7695–1950–4/03, 2003.

912
913 ~~He, F., Liu, T., Tao, D.: Control batch size and learning rate to generalize well: theoretical and empirical evidence.
914 Neural Information Processing Systems, 2019.~~

915
916 Ibbeken, H., and Schleyer, R.: Photo-sieving: A method for grain-size analysis of coarse-grained, unconsolidated
917 bedding surfaces. Earth Surf. Process. Landforms, 11, 59–77. Available at:
918 <https://doi.org/10.1002/esp.3290110108>, 1986.

919
920 Igathinathane, C., Melin, S., Sokhansanj, S., Bi, X., Lim, C. J., Pordesimo, L. O. and Columbus, E. P.: Machine
921 vision based particle size and size distribution determination of airborne dust particles of wood and bark pellets.
922 Powder Technol., 196, 202–212. Available at: <https://doi.org/10.1016/j.powtec.2009.07.024>, 2009.

923
924 Kellerhals, R. and Bray, D. I.: Sampling Procedures for Coarse Fluvial Sediments. J. Hydraul. Div., 97, 1165–
925 1180., 1971.

926
927 Kim, H., Han, J. and Han, T. Y.: Machine vision-driven automatic recognition of particle size and morphology in
928 SEM images. Nanoscale, 12, 19461–19469. Available at: <https://doi.org/10.1039/D0NR04140H>, 2020.

929
930 ~~Kinsman, N.: Single-Beam Bathymetry Data Collected in Shallow-Water Areas near Gambell, Golovin, Hooper
931 Bay, Savoonga, Shishmaref, and Wales, Alaska 2012–2013; Department of Natural Resources. Division of
932 Geological & Geophysical Surveys: Fairbanks, AK, USA, 2015.~~

933
934 Le, Q. V.: Building high-level features using large scale unsupervised learning. In Proceedings of the 2013 IEEE
935 International Conference on Acoustics, Speech and Signal Processing, Vancouver, BC, Canada, pp. 8595–8598.,
936 2013.
937
938 Leopold, L. B.: An Improved Method for Size Distribution of Stream Bed Gravel. *Water Resour. Res.*, 6, 1357–
939 1366. <https://doi.org/10.1029/WR006i005p01357>, 1970.
940
941 Limare, A., Tal, M., Reitz, M. D., Lajeunesse, E., and Métivier, F.: Optical method for measuring bed topography
942 and flow depth in an experimental flume. *Solid Earth*, 2, 143–154, <https://doi.org/10.5194/se-2-143-2011>, 2011.
943
944 Lowe, D. G.: Distinctive Image Features from Scale-Invariant Keypoints. *International Journal of Computer
945 Vision*, 60, pages 91–110, 2004.
946
947 Lu, S., Gao, F., Piao, Ch. and Ma, Y.: Dynamic Weighted Cross Entropy for Semantic Segmentation with
948 Extremely Imbalanced Data. 2019 International Conference on Artificial Intelligence and Advanced
949 Manufacturing (AIAM). doi: 10.1109/AIAM48774.2019.00053, 2019.
950
951 Mueller D. S., Wagner, Ch. R.: Measuring Discharge with Acoustic Doppler Current Profilers from a Moving
952 Boat. USGS, Chapter 22 of Book 3, Section A. <https://pubs.usgs.gov/tm/3a22/>, 2009.
953
954 Mueller D. S., Wagner, Ch. R.: Measuring discharge with acoustic Doppler current profilers from a moving boat,
955 version 2.0. [https://www.researchgate.net/publication/284587353_Measuring_discharge_with_acoustic_-_](https://www.researchgate.net/publication/284587353_Measuring_discharge_with_acoustic_-_Doppler_current_profilers_from_a_moving_boat)
956 [Doppler current profilers from a moving boat](https://www.researchgate.net/publication/284587353_Measuring_discharge_with_acoustic_-_Doppler_current_profilers_from_a_moving_boat), 2013.
957
958 Muste, M., Baranya, S., Tsubaki, R., Kim, D., Ho, H., Tsai, H. and Law, D.: Acoustic mapping velocimetry. *Water
959 Resour. Res.*, 52, 4132–4150, doi:10.1002/2015WR018354., 2016.
960
961 Obodovskiy, O., Habel, M., Szatten, D., Rozlach, Z., Babiński, Z., Maerker, M.: Assessment of the Dnieper
962 Alluvial Riverbed Stability Affected by Intervention Discharge Downstream of Kaniv Dam. *Water*, 12(4):1104.
963 <https://doi.org/10.3390/w12041104>, 2020.
964
965 Padilla, R., Netto, S. M. and da Silva, E. A. B.: A Survey on Performance Metrics for Object-Detection
966 Algorithms. Conference: 2020 International Conference on Systems, Signals and Image Processing (IWSSIP).
967 DOI: 10.1109/IWSSIP48289.2020, 2020.
968
969 Perez, L. and Wang, J.: The Effectiveness of Data Augmentation in Image Classification using Deep Learning.
970 arXiv preprint arXiv:1712.04621. Av. at: <https://arxiv.org/abs/1712.04621>, 2017., 2017.
971
972 Purinton, B. and Bookhagen, B.: Introducing PebbleCounts: A grain-sizing tool for photo surveys of dynamic
973 gravel-bed rivers. *Earth Surf. Dyn.*, 7, 859–877. <https://doi.org/10.5194/esurf-7-859-2019>, 2019.
974
975 Rákóczi, L.: Selective erosion of noncohesive bed materials. *Geografiska Annaler. Series A, Physical Geography*,
976 Vol. 69, No. 1, pp. 29-35. <https://doi.org/10.2307/521364>, 1987.
977
978 Rákóczi, L.: Identification of river channel areas inclined for colmation, based on the analysis of bed material.
979 *Vizügyi Közlemények, LXXIX.*, chapter 3., 1997.
980
981 Rahman, M. A. and Wang, Y.: Optimizing Intersection-Over-Union in Deep Neural Networks for Image
982 Segmentation. In: *Bebis G. et al. (eds) Advances in Visual Computing. ISVC 2016. Lecture Notes in Computer
983 Science*, vol 10072. Springer, Cham. https://doi.org/10.1007/978-3-319-50835-1_22, 2016.
984
985 RD Instruments – Acoustic Doppler Current Profilers – Application Note: https://www.commtec.com/library/Technical_Paper/Manuscripts/RDI/FSA-004%20Model1.pdf, 1999.
986
987
988 Rice, S. and Church, M.: Grain size along two gravel-bed rivers: Statistical variation, spatial pattern and
989 sedimentary links. *Earth Surf. Process. Landf.*, 23, 345–363., 1998.
990

991 Ren, H., Hou, Z., Duan, Z., Song, X., Perkins, W.A., Richmond, M. C., Arntzen, E. V. and Scheibe, T. D.: Spatial
992 Mapping of Riverbed Grain-Size Distribution Using Machine Learning. *Front. Water*, 2:551627. doi:
993 10.3389/frwa.2020.551627, 2020.

994
995 Rozniak, A., Schindler, K., Wegner, J. D. and Lang, N.: Drone images and Deep Learning for river monitoring in
996 Switzerland. Semester project. Institute of Geodesy and Photogrammetry, Project, Swiss Federal Institute of
997 Technology (ETH) Zurich, 2019.

998
999 Rubin, D. M.: A simple autocorrelation algorithm for determining grain-size from digital images of sediment. *J.*
1000 *Sed. Res.*, 74, 160–165., 2004.

1001
1002 Rubin, D. M., Chezar, H., Harney, J. N., Topping, D. J., Melis, T. S., Sherwood, C. R.: Underwater microscope
1003 for measuring spatial and temporal changes in bed-sediment grain size. *Sedimentary Geology*, Volume 202, Issue
1004 3, Pages 402-408, <https://doi.org/10.1016/j.sedgeo.2007.03.020>, 2007.

1005
1006 Scheder, C., Lerchegger, B., Flödl, P., Csar, D., Gumpinger, C. and Hauer, C.: ~~River-bed~~~~Riverbed~~ stability versus
1007 clogged interstitial: Depth-dependent accumulation of substances in freshwater pearl mussel (*Margaritifera*
1008 *margaritifera* L.) habitats in Austrian streams as a function of hydromorphological parameters. *Limnologia*,
1009 Volume 50, January 2015, Pages 29-39. <https://doi.org/10.1016/j.limno.2014.08.003>, 2015.

1010
1011 Shields, F. D., Jr. and Rigby, J. R.: River habitat quality from river velocities measured using acoustic Doppler
1012 current profiler. *Environ. Manage.*; 36(4):565-75. doi: 10.1007/s00267-004-0292-6., 2005.

1013
1014 Shields, F. D. Jr.: Aquatic Habitat Bottom Classification Using ADCP. *Journal of Hydraulic Engineering*, Vol.
1015 136, Issue 5, 2010.

1016
1017 Sime, L. C. and Ferguson, R. I.: Information on grain-sizes in gravel bed rivers by automated image analysis. *J.*
1018 *Sed. Res.*, 73, 630–636., 2003.

1019
1020 Simpson, M. R.: Discharge Measurements Using a Broad-Band Acoustic Doppler Current Profiler. USGS, Open-
1021 File Report 01-1, <https://pubs.usgs.gov/of/2001/ofr0101/>, 2002.

1022
1023 Singer, M. B.: A new sampler for extracting bed material sediment from sand and gravel beds in navigable rivers.
1024 *Earth Surface Processes and Landforms* 33(14):2277 – 2284 DOI: 10.1002/esp.1661, 2008.

1025
1026 Soloy, A., Turki, I., Fournier, M., Costa, S., Peuziat, B. and Lecoq, N.: A Deep Learning-Based Method for
1027 Quantifying and Mapping the Grain Size on Pebble Beaches. *Remote Sens.*, 12, 3659, doi:10.3390/rs12213659,
1028 2020.

1029
1030 Staudt, F., Mullarney, J. C, Pilditch, C. A. and Huhn, K.: Effects of grain-size distribution and shape on sediment
1031 bed stability, near-bed flow and bed microstructure. *Earth Surface Processes and Landforms*, 44(5). DOI:
1032 10.1002/esp.4559, 2018.

1033
1034 Sun, Z., Zheng, H. and Sun, L.: Analysis on the Characteristics of Bed Materials in the Jinghong Reservoir on the
1035 Lancang River. *Sustainability*, 13, 6874. <https://doi.org/10.3390/su13126874>, 2021.

1036
1037 Takechi, H., Aragaki, S. and Irie, M.: Differentiation of River Sediments Fractions in UAV Aerial Images by
1038 Convolution Neural Network. *Remote Sens.*, 13, 3188. <https://doi.org/10.3390/rs13163188>, 2021.

1039
1040 Taravat, A., Wagner, M. P., Bonifacio, R. and Petit, D.: Advanced Fully Convolutional Networks for Agricultural
1041 Field Boundary Detection. *Remote Sens.*, 13, 722., 2021.

1042
1043 Török, G. T., Baranya, S. (2017) Morphological Investigation of a Critical Reach of the Upper Hungarian Danube.
1044 *Periodica Polytechnica Civil Engineering*. 61(4), pp. 752–761. <https://doi.org/10.3311/PPci.10530>, 2017.

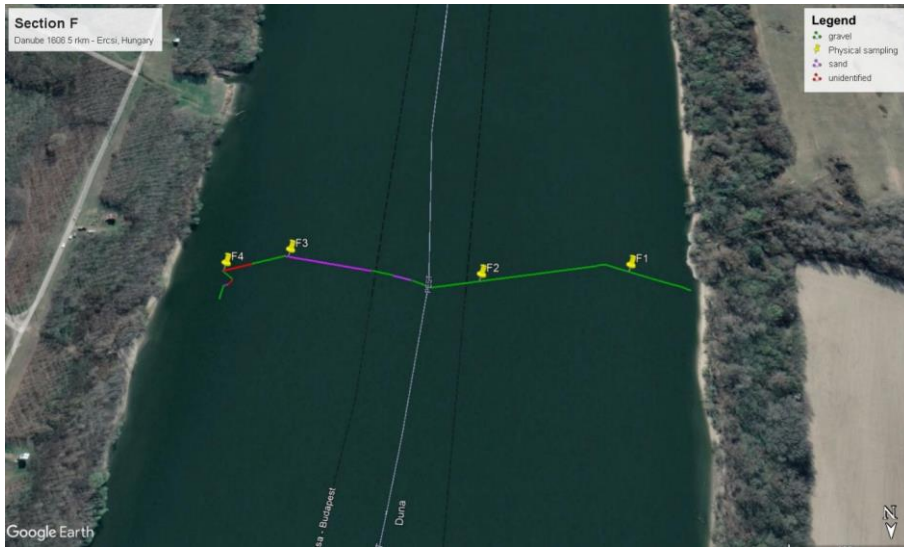
1045
1046 ~~Török, G. T., Baranya, S. and Rütger, N.: 3D-CFD Modeling of Local Scouring, Bed Armoring and Sediment~~
1047 ~~Deposition. *Water*, 9(1), 56. <https://doi.org/10.3390/w9010056>, 2017.~~

1048
1049
1050 USDA: Guidelines for Sampling Bed Material. Technical Supplement 13A, 2007.

1051
1052 Vanoni, V. A. and Hwang, L. S.: Relation between Bed Forms and Friction in Streams. *J. Hydraulics Division.*,
1053 93 (3), 121–144. doi:10.1061/JYCEAJ.0001607, 1967.
1054
1055 Verdú, J. M., Batalla, R. J. and Martínez-Casanovas, J. A.: High-resolution grain-size characterisation of gravel
1056 bars using imagery analysis and geo-statistics. *Geomorphology*, 72, 73–93., 2005.
1057
1058 Warrick, J. A., Rubin, D. M., Ruggiero, P., Harney, J. N., Draut, A. E. and Buscombe, D.: Cobble cam: Grain-
1059 size measurements of sand to boulder from digital photographs and autocorrelation analyses. *Earth Surf. Process*
1060 *Landf.*, 34, 1811–1821. <https://doi.org/10.1002/esp.1877>, 2009.
1061
1062 Wilcock, P. R.: Persistence of armor layers in gravel-bed streams. *Hydrology and Land Surface Studies.*
1063 <https://doi.org/10.1029/2004GL021772>, 2005.
1064
1065 Wolcott, J. F., Church, M.: Strategies for sampling spatially heterogeneous phenomena: The example of river
1066 gravels. *Journal of Sedimentary Research*. v. 61, no. 4, p. 534–543, 1991.
1067
1068 WMO: Measurement of river sediments: prepared by the Rapporteur on Sediment Transport of the Commission
1069 for Hydrology. Report, World Meteorological Organization - No. 561, Operational hydrology report (OHR)- No.
1070 16, 1981.
1071
1072 Yang, F., Yi, M., Cai, Y., Blasch, E., Sullivan, N., Sheaff, C., Chen, G. and Ling, H.: Multitask Assessment of
1073 Roads and Vehicles Network (MARVN). Proceedings Volume 10641, Sensors and Systems for Space
1074 Applications XI, 106410D, <https://doi.org/10.1117/12.2305972>, 2018.
1075
1076 [You, K., Long, M., Wang, J., Jordan M.I.: How Does Learning Rate Decay Help Modern Neural Networks?](https://doi.org/10.48550/arXiv.1908.01878)
1077 <https://doi.org/10.48550/arXiv.1908.01878>, 2019.
1078
1079 Yu, L., Wang, S. and Lai, K.K.: Data Preparation in Neural Network Data Analysis. In book: Foreign-Exchange-
1080 Rate Forecasting with Artificial Neural Networks. DOI: 10.1007/978-0-387-71720-3_3, 2007.
1081
1082 Zamir, A. R., Sax, A., Shen, W., Guibas, L., Malik, J. and Savarese, S.: Taskonomy: Disentangling Task Transfer
1083 Learning. In Proceedings of the 2018 IEEE/CVF Conf. on Computer Vision and Pattern Recognition, Salt Lake
1084 City, UT, USA, pp. 3712–3722. doi: 10.1109/CVPR.2018.00391, 2018.
1085
1086 Zhang, Q., Shi, Y., Chen, Z. and Jiang, T.: ADCP measured flow current of the middle-lower Changjiang River
1087 channel. *Front. Earth Sci., China* 2, 1–9. <https://doi.org/10.1007/s11707-008-0016-y>, 2008.
1088
1089 Zhou, Y., Lu, J., Jin, Z., Li, Y., Gao, Y., Liu, Y. and Chen, P.: Experimental Study on the Riverbed Coarsening
1090 Process and Changes in the Flow Structure and Resistance in the Gravel Riverbed Downstream of Dams. *Front.*
1091 *Environ. Sci.*, <https://doi.org/10.3389/fenvs.2021.611668>, 2021.
1092
1093 Zhu, J., Park, T., Isola, P. and Efros, A. A.: Unpaired Image-to-Image Translation using Cycle-Consistent
1094 Adversarial Networks. arxiv, <https://arxiv.org/abs/1703.10593>, 2020.
1095

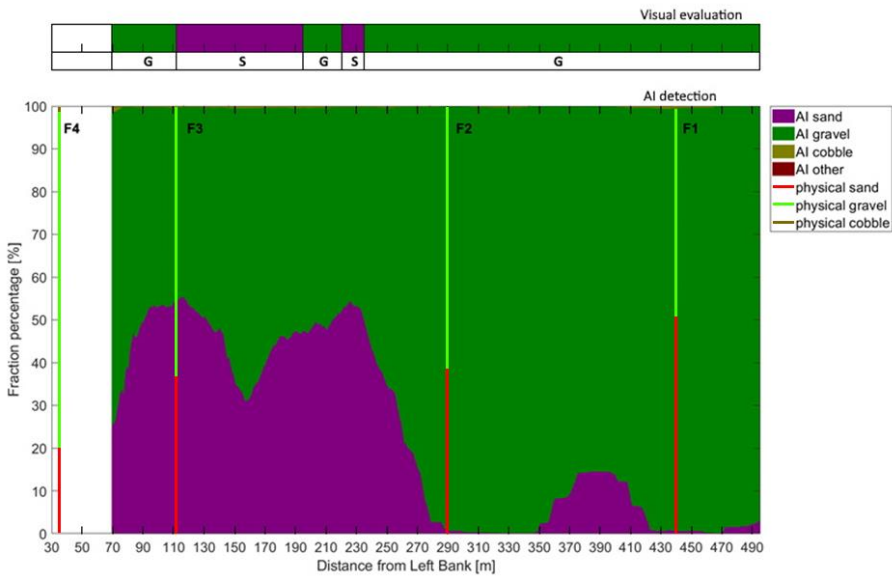
1096 Appendix

1097 Appendix A Site A - Section F

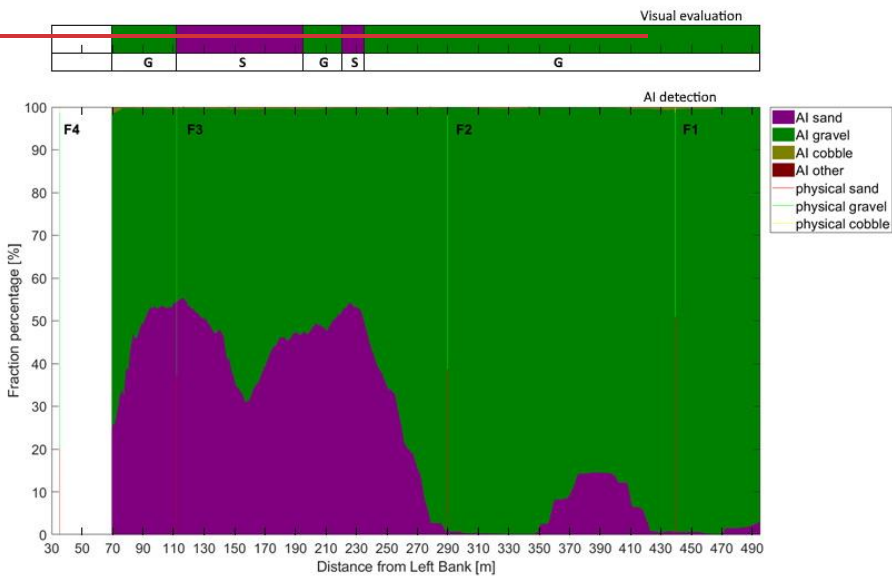


1098 Figure A1: The path of the vessel and camera in Section F, Site A. The polyline is coloured based on the sediment seen
1099 during visual evaluation of the video. Yellow markers are the locations of physical bed material samplings. (Map
1100 created with Google Earth Pro)
1101

1102



1103



1104

1105

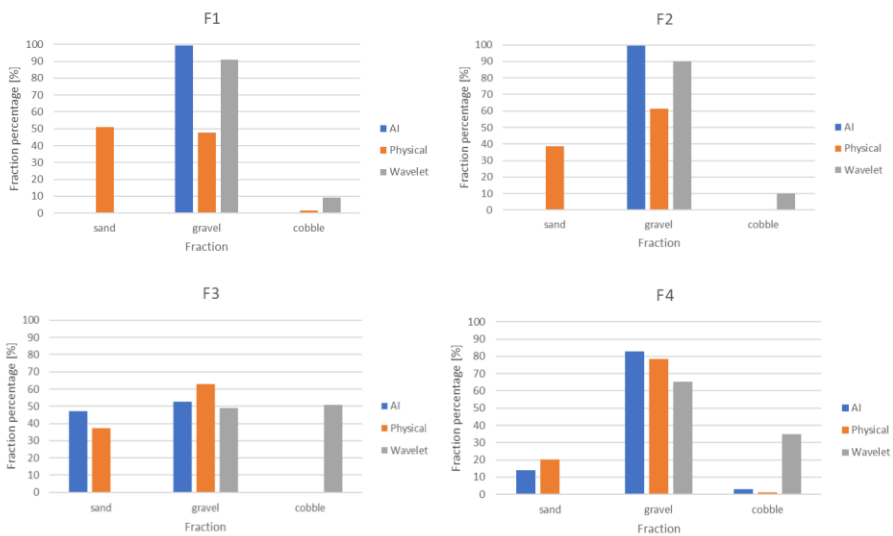
1106

1107

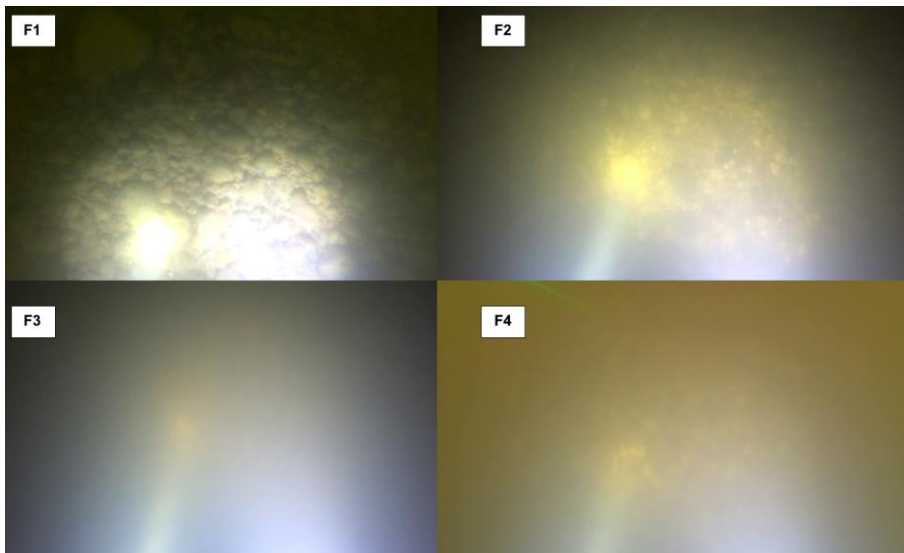
Figure A2: Sediment fraction percentages in Section F, recognised by the AI. The visual evaluation included two classes: gravel – G, sand – S). The fractions of the physical samples are shown as verticals. The fractions from the physical samples are also shown (verticals).

1108

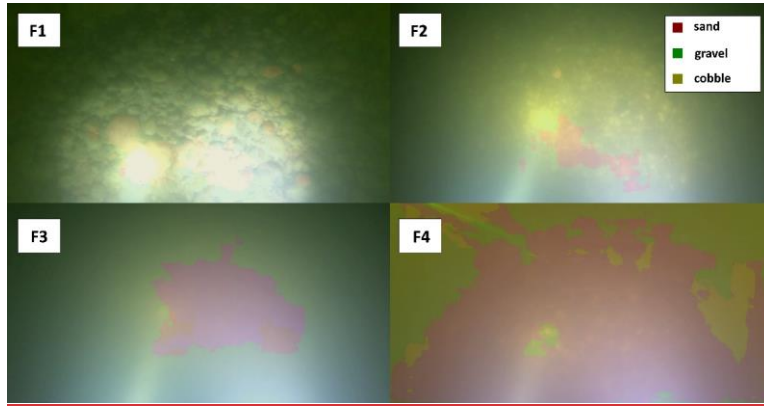
1109



1110
1111
1112 **Figure A3: Comparison of sediment fraction % at the sampling locations from the moving-averaged AI detection, conventional sieving and the wavelet-based image processing method. Section F.**



1113
1114
1115 **Figure A4: Riverbed video images at the sampling points in Section F.**



1116
1117

Figure A5: Riverbed video images overlapped with their raw, AI detection result, at the sampling points in Section F.

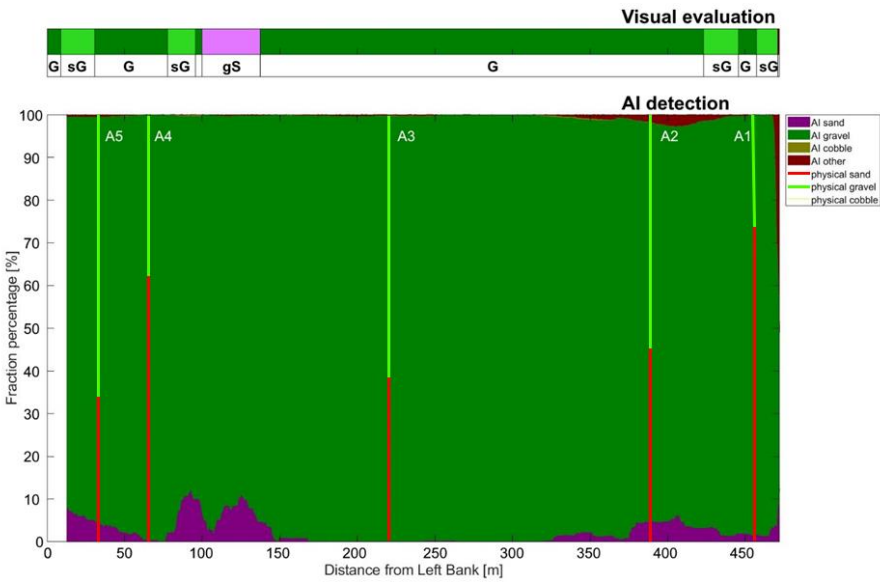
1118 Appendix B Site A – Section A



1119 Figure B1: The path of the vessel and camera in Section A, Site A. The polyline is coloured based on the sediment seen
1120 during visual evaluation of the video. Yellow markers are the locations of physical bed material samplings. (Map
1121 created with Google Earth Pro)
1122

1123

1124



1125
1126
1127
1128

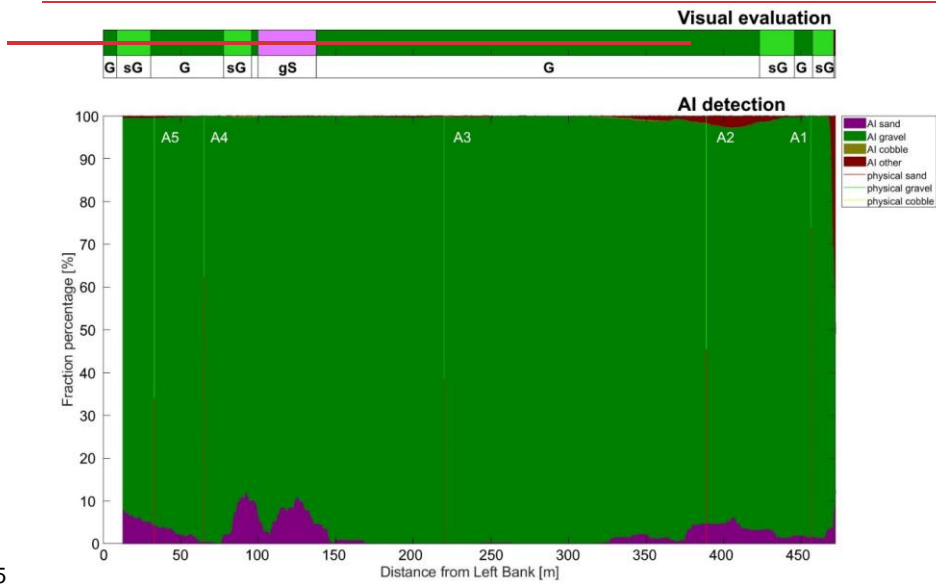
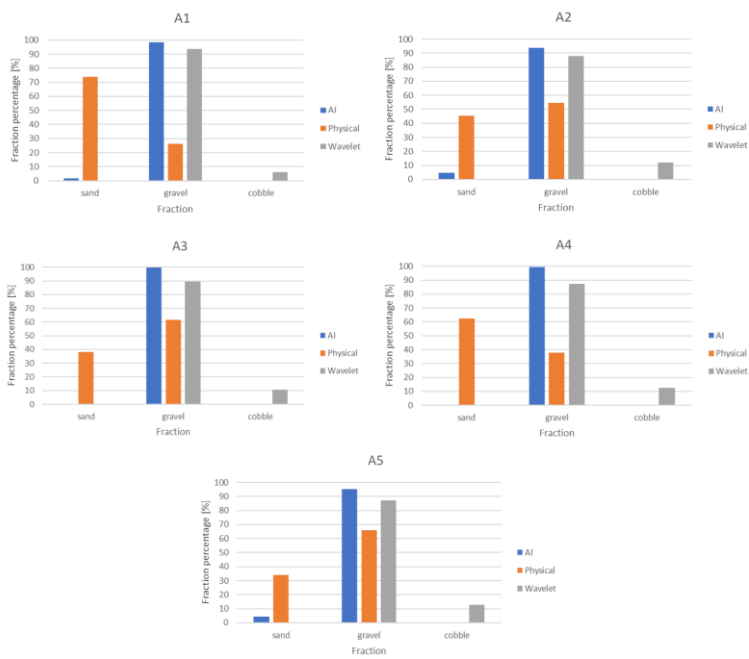
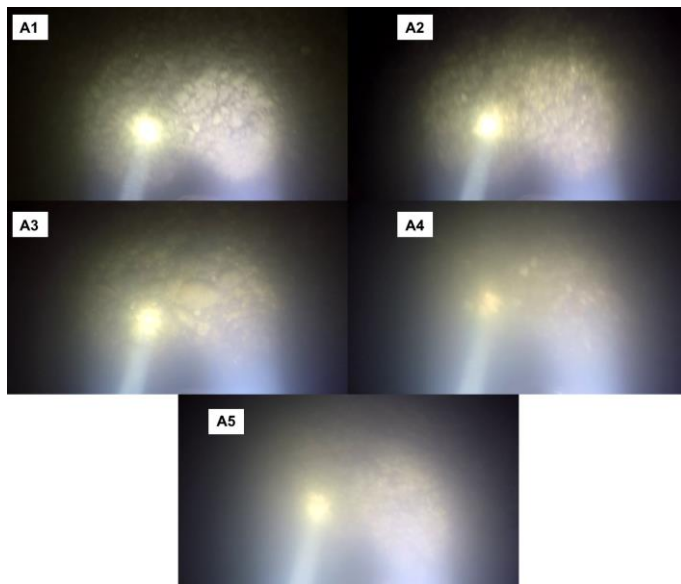


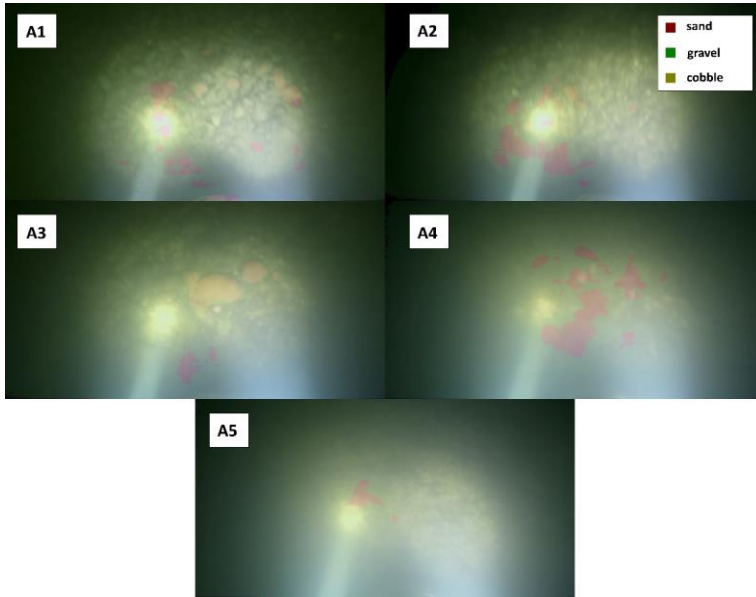
Figure B2: Sediment fraction percentages in Section A, recognised by the AI. The visual evaluation included three classes: gravel – G, sandy gravel – sG, gravelly sand - gS). The fractions of the physical samples are shown as verticals. The fractions from the physical samples are also shown (verticals).



1129
1130
1131 **Figure B3: Comparison of sediment fraction % at the sampling locations from the moving-averaged AI detection, conventional sieving and the wavelet-based image processing method. Section A.**



1132
1133
1134 **Figure B4: Riverbed video images at the sampling points in Section A.**

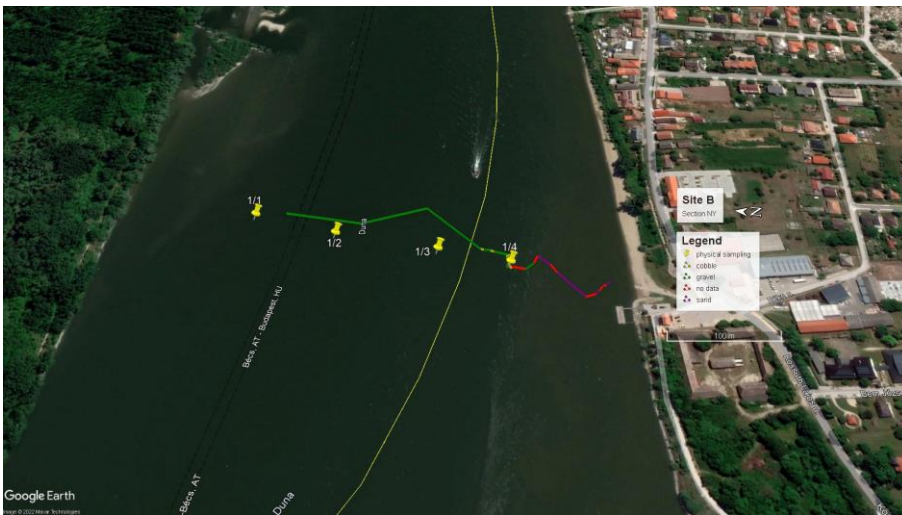


1135
1136
1137

Figure B5: Riverbed video images overlapped with their raw, AI detection result, at the sampling points in Section F.

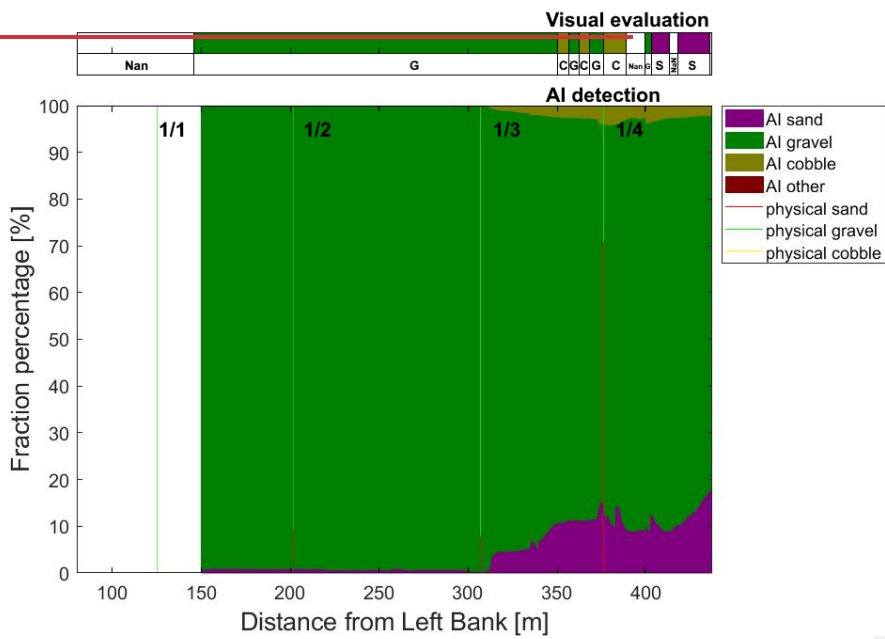
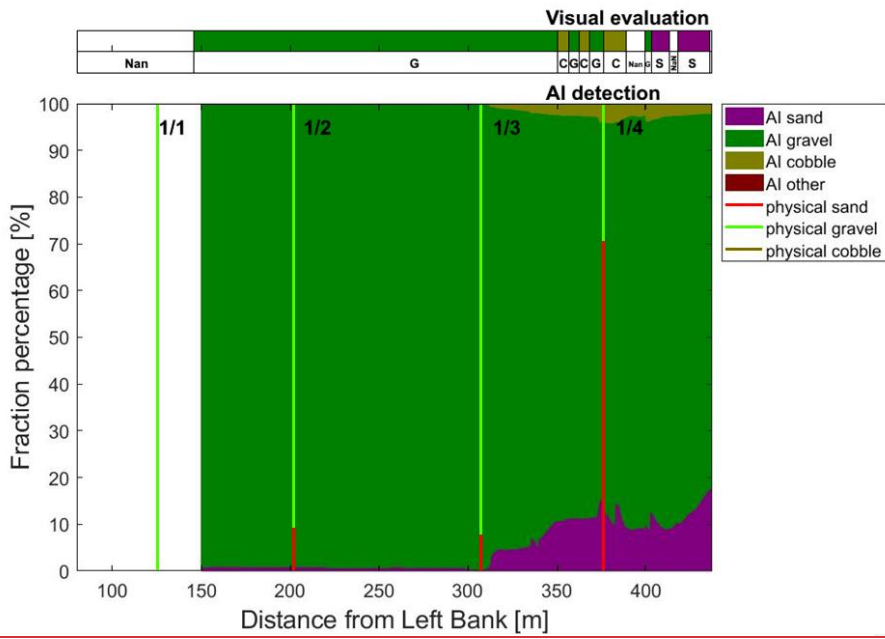
- Formatted: Font: 9 pt
- Formatted: Font: 9 pt
- Formatted: Font: (Default) Arial, Not Bold, Italic
- Formatted: Normal

1138 Appendix C Site B – Section NY



1139
1140
1141
1142

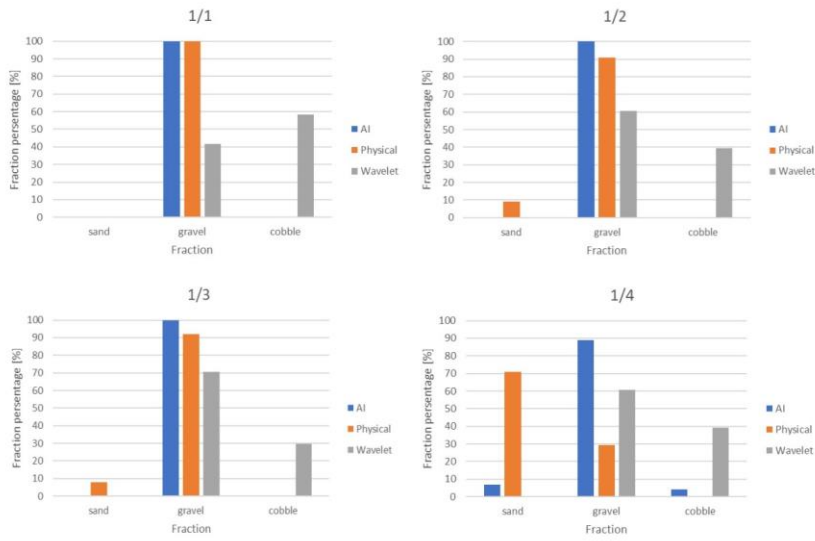
Figure C1: The path of the vessel and camera in Section NY, Site B. The polyline is coloured based on the sediment seen during visual evaluation of the video. Yellow markers are the locations of physical bed material samplings. (Map created with Google Earth Pro)



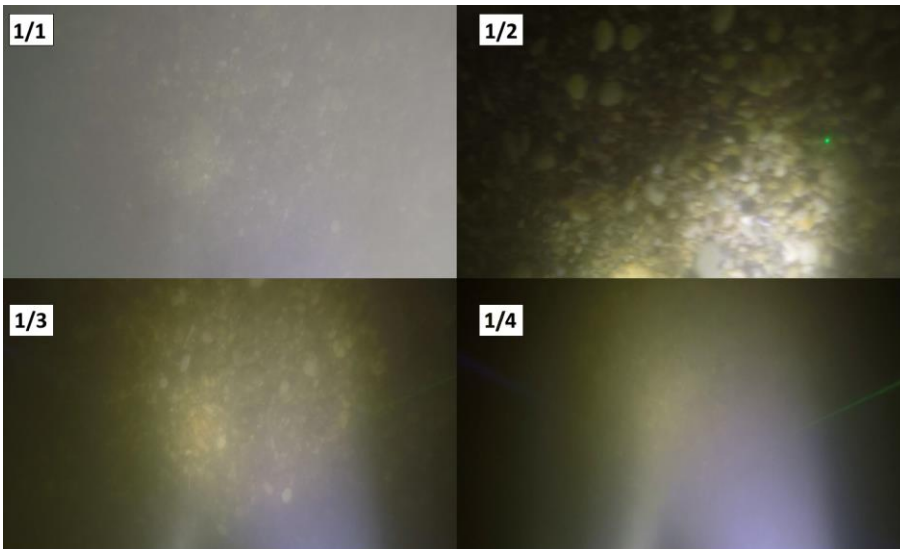
1143

1144
1145
1146
1147

Figure C2: Sediment fraction percentages in Section NY, recognised by the AI. The visual evaluation included two classes: gravel – G, sand – S). The fractions of the physical samples are shown as verticals. The fractions from the physical samples are also shown (verticals).

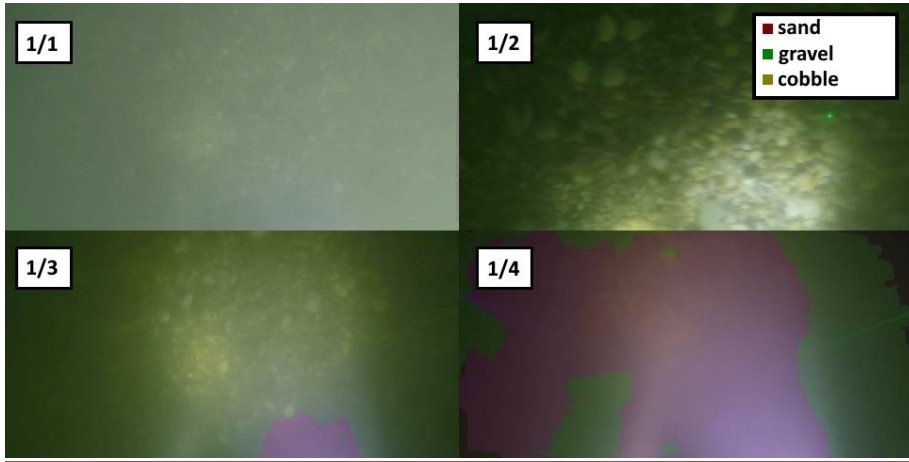


1148
1149 **Figure C3: Comparison of sediment fraction % at the sampling locations from the moving-averaged AI detection,**
1150 **conventional sieving and the wavelet-based image processing method. Section NY.**



1151
1152 **Figure C4: ~~River-bed~~Riverbed video images at the sampling points in Section NY.**

1153



1154
1155
1156

Figure C5: Riverbed video images overlapped with their raw, AI detection result, at the sampling points in Section NY.

Formatted: Normal, Left

Formatted: Font: 9 pt